



저작자표시-비영리-변경금지 2.0 대한민국

이용자는 아래의 조건을 따르는 경우에 한하여 자유롭게

- 이 저작물을 복제, 배포, 전송, 전시, 공연 및 방송할 수 있습니다.

다음과 같은 조건을 따라야 합니다:



저작자표시. 귀하는 원저작자를 표시하여야 합니다.



비영리. 귀하는 이 저작물을 영리 목적으로 이용할 수 없습니다.



변경금지. 귀하는 이 저작물을 개작, 변형 또는 가공할 수 없습니다.

- 귀하는, 이 저작물의 재이용이나 배포의 경우, 이 저작물에 적용된 이용허락조건을 명확하게 나타내어야 합니다.
- 저작권자로부터 별도의 허가를 받으면 이러한 조건들은 적용되지 않습니다.

저작권법에 따른 이용자의 권리는 위의 내용에 의하여 영향을 받지 않습니다.

이것은 [이용허락규약\(Legal Code\)](#)을 이해하기 쉽게 요약한 것입니다.

[Disclaimer](#)

공학석사 학위논문

Applications of Computational Fluid Dynamics in Violent Water-Impact Problems

격렬한 수면충격 문제에 대한 전산

유체 역학 적용

2016년 8월

서울대학교 대학원

조선해양공학과

주 장

Applications of Computational Fluid Dynamics in Violent Water-Impact Problems

지도 교수 김 용 환

이 논문을 공학석사 학위논문으로 제출함

2016년 7월

서울대학교 대학원

조선해양공학과

주 장

주장의 석사학위논문을 인준함

2016년 7월

위 원 장 _____ (인)

부위원장 _____ (인)

위 원 _____ (인)

Abstract

Applications of Computational Fluid Dynamics in Violent Water-Impact Problems

Zhang Zhu

Department of Naval Architecture and Ocean Engineering

The Graduate School

Seoul National University

Slosh-induced impact and water-entry impact are two typical cases of violent water-impact that causes highly distorting free-surface and large loads in transient time. Extensive studies have been carried out by experiments and potential theories in the past decades. This thesis has investigated the applications of a commercial computational fluid dynamics (CFD) code, Star-CCM+, in sloshing and water-entry problems.

In sloshing problem, computation efficiency of adaptive mesh models was observed before carrying out parametric sensitivity study. Several mesh models were designed by different refinements around impact region. It has shown that an efficient mesh model with appropriate numerical conditions reduces computation time significantly and produces similar pressure signals and free-surface shapes with experiment.

Then, two-dimensional ship-like sections were studied in water-entry problems. Appropriate overlapping meshes were arranged so that the section can move inside

computational domain without losing numerical stability. Moreover, in order to compare with the analytical solutions which have been developed based on high Froude number (F_n) condition, F_n effect was also investigated and CFD computation showed reasonable performance. The CFD analysis has presented reasonable agreement in impact loads and free-surface developments with analytical solutions and experiments

Water-entry study was then extended to a 3-D modified Wigley case. Impact characteristic was found that both maximum body acceleration and maximum impact force are linear proportional to drop height. Moreover, the peak impact force occurs at the same water-entry depth, which is independent of drop height.

These results show that CFD analysis is becoming matured for engineering application nowadays.

Keywords: CFD, Violent water-impact, sloshing, water-entry

Student Number: 2014-25273

Contents

Chapter 1 Introduction.....	1
1.1 Research Motivations	1
1.2 State of the Art	2
1.2.1 Sloshing problem.....	2
1.2.2 Water-entry problem	3
Chapter 2 Numerical Method	5
2.1 Governing Equations	5
2.2 Numerical Models.....	6
Chapter 3 Slosh Problem.....	7
3.1 Computational Model	7
3.2 Parametric Sensitivity Study.....	9
3.2.1 Solution Grids: Adaptive Meshes	9
3.2.2 Sensitivity to Spatial Discretization	13
3.2.3 Sensitivity to Temporal Discretization.....	17
3.3 Results and Discussions.....	20
Chapter 4 2-D Water-Entry Problem of Wedge and Ship-Like Sections.....	24
4.1 Computational Models.....	24
4.2 Parametric Sensitivity Study.....	27
4.2.1 Sensitivity to Mesh Models.....	27
4.2.2 Sensitivity to Time Step	30
4.2.3 Sensitivity to Grid Size	31

4.3 Results and Discussions.....	36
Chapter 5 Water-Entry Problem of a 3-D Modified Wigley	49
5.1 Model Introduction	49
5.2 Results and Discussions.....	52
Chapter 6 Conclusions.....	55
Bibliography	57

List of Tables

Table 3.1 Number of grids for mesh models with different $L/\Delta x_{min}$ (unit: million)...	9
Table 3.2 Main specifications of processor	11
Table 3.3 Computational time for each mesh model (unit: hour).....	11
Table 4. 1 Drop conditions	26
Table 4. 2 Four computation cases with different time steps	30
Table 4. 3 GCI estimations for peak values of pressure and force	36
Table 4. 4 Four cases with different Fn conditions	37
Table 5. 1 Hull geometry.....	50
Table 5. 2 Numerical conditions for CFD computation	51

List of Figures

Fig. 3. 1 Schematic view of tank and probe points	8
Fig. 3. 2 Snapshots of free surface shapes during impact	8
Fig. 3. 3 Three types of adaptive mesh models	10
Fig. 3. 4 Comparison of pressure signals	12
Fig. 3. 5 Sequential snapshots of free-surface development at right tank ceiling ...	13
Fig. 3. 6 Pressure signals on four probe points	16
Fig. 3. 7 Pressure peak values over $L/\Delta x_{min}$	17
Fig. 3. 8 Pressure signals obtained by different temporal schemes and time steps .	19
Fig. 3. 9 Comparison of pressure signals between PIV test and CFD computation	21
Fig. 3. 10 Snapshots of free-surface development and velocity vector at right tank ceiling.....	23
Fig. 4. 1 Geometry of two ship-like sections	25

Fig. 4. 2 Computation domain (half) and boundary conditions	26
Fig. 4. 3 Two examples of data mapping at inial computation stage	29
Fig. 4. 4 Pressure time signals for different cases	30
Fig. 4. 5 Comparison of original data and filtered data.....	31
Fig. 4. 6 Results using different grid resolutions	33
Fig. 4. 7 Time signals by different grid resolutions.....	35
Fig. 4. 8 Pressure signals on P1.....	37
Fig. 4. 9 Pressure distribution on wedge bottom and free-surface shapes at three instants.....	38
Fig. 4. 10 Comparison of time signals (wedge section, tilting angle: 0).....	41
Fig. 4. 11 Comparison of free-surface shapes (wedge section, tilting angle: 0).....	42
Fig. 4. 12 Comparison of time signals (wedge section, tilting angle: 30°).....	43
Fig. 4. 13 Comparison of free-surface shapes (wedge section, tilting angle: 30°) ..	44
Fig. 4. 14 Comparison of time signals (ship section, drop height: 0.17m)	45
Fig. 4. 15 Comparison of free-surface shapes (ship section, drop height: 0.17m) ..	46
Fig. 4. 16 Comparison of time signals (ship section, drop height: 0.30m)	47
Fig. 4. 17 Comparison of free-surface shapes (ship section, drop height: 0.30m) ..	48
Fig. 5. 1 Configuration of modified Wigley	50
Fig. 5. 2 Part of mesh model that around hull	51
Fig. 5. 3 Time signals by different drop heights (H)	53
Fig. 5. 4 Relationship between maximum value and drop height	54

Chapter 1 Introduction

1.1 Research Motivations

Violent water-impact is defined as a strong fluid-structure interaction that is characterized by high nonlinearity, distorting free surface and large structure response in transient duration. Common examples of this problem are liquid sloshing in tank, water-entry of hull, green water on decks and so on. These phenomena frequently occur and cause severe structure damage to ships and structures that operate in ocean environment. Experiment has been the main tool for observing these complicated phenomena in the past decades, but the high cost and limited facilities somehow restrict the research. Many researchers have developed analytical solutions by using simple model, but their works become difficult when considering complicated conditions, e.g. arbitrary geometry, highly distorting free surface, trapping air and so on. However, as the rapid increase of computation capacity, CFD technique that could handle with complicated fluid phenomena is becoming popular nowadays. Main objectives of this thesis are observing the characteristics of violent water-impact problems such as sloshing and water-entry, investigating into sensitivity of numerical parameters, and verifying CFD method as a practical engineering tool for studying violent water-impact problems.

1.2 State of the Art

1.2.1 Sloshing problem

Slosh-induced impact widely occurs in the LNG related ships and offshore structures. It has been understood as a stochastic phenomenon, thus statistical analysis is essential to assess the sloshing impacts. Numerous experiments have been carried out to observe this complicated phenomenon (e.g. Kuo *et al.*, 2009; Kim *et al.*, 2012). To identify the relationship between velocity and pressure for sloshing impact phenomena, particle image velocimetry (PIV) technique becomes an important tool and has been applied in the experiments. Recently, Yang *et al.* (2015) conducted PIV test on the sloshing model, which provides validation data for the CFD analysis in this thesis.

In another way, many numerical studies on sloshing flows have been also reported in the past and being reported in the present. Kim (2001) simulated the sloshing flows based on a finite difference method. He introduced a concept of buffer zone that locates near the tank ceiling, and observed the averaged impact over several time steps.

Lee *et al.* (2007) carried out a series of parametric sensitivity studies on tank sloshing loads by using a commercial program, FLOW3D. They adopted Froude scaling law, and observed the sensitivity of impact pressure against physical parameters, such as fluid viscosity, liquid–gas density ratio, and ullage pressure and compressibility.

Yang *et al.* (2015) applied a constrained-interpolation-profile (CIP) method for the analysis of impact characteristics of sloshing phenomenon. They applied the same model, which was analyzed in this thesis.

1.2.2 Water-entry problem

The pioneering study on water-entry phenomena was proposed by von Karman (1929). Based on potential theory and assumption of plate section, Karman developed a solution for the flat and near flat impact problems with linearized free surface and body boundary conditions. Wagner (1932) continued Karman's solution by accounting for the pile-up of water, applying dynamics boundary condition on upraised free surface rather than calm free surface. This is key modification of Karman's method. However, many theories and experiments showed that Karman solution gives a relatively low prediction of impact pressure while Wagner method provides too large prediction.

Zhao and Faltinsen (1993) generalized the work of Wagner on arbitrary cross-sections by using nonlinear boundary element method. This numerical method was verified by comparison with a new similarity solution that was derived for wedges with deadrise angle from 4° to 81° . Moreover, an asymptotic solution had been derived for pressure on wedge and shown good agreement with both the similarity solution and BEM method for small deadrise angles.

In 2014, the Wave Induced Loads on Ships Joint Industry Project (WILS JIP) carried out the investigation of the slamming and whipping phenomena in ocean environment. As a participant of WILS JIP, Korea Research Institute of Ships & Ocean Engineering (KRISO) performed a series of model tests for wave-induced impact loads on ships. The project also observed the drop characteristics of 2-D wedge and 2-D ship sections, providing validation data for the CFD analysis in this thesis.

Kim *et al.* (2016) summarized a comparative study on water-entry impact problem

by using potential theories and CFD computations. They applied two potential methods, generalized Wagner model (GWM) and modified Logvinovich model (MLM) for the analysis. The GWM is expressed in Zhao and Faltinsen (1993), and the Modified Logvinovich model (MLM) is based on the original Wagner model (OWM) and the original Logvinovich model (OLM) with an improvement. The improvement is achieved by adding an extra term to the velocity potential.

Chapter 2 Numerical Method

Computational fluid dynamics (CFD) is a branch of fluid mechanics that uses numerical analysis and algorithms to deal with problems that involve fluid dynamics. This study employs the commercial CFD program, Star-CCM+, to simulate the water-impact problems and investigate numerical sensitivities.

2.1 Governing Equations

Continuity, momentum, and energy equations are three fundamental governing equations that are also known as transport equations. A general form (Eq. 2.1) can be derived for a general quantity ϕ by the commonality between the transport equations. The terms in Eq. 2.1 are, from left to right, the transient term, the convection term, the viscous term, and the source term. ρ is flow density, \mathbf{u} is velocity vector, Γ is diffusivity and S_ϕ is source momentum.

$$\frac{\partial(\rho\phi)}{\partial t} + \nabla(\rho\phi\mathbf{u}) = \nabla(\Gamma\nabla\phi) + S_\phi \quad (2.1)$$

However, the study of this thesis only considers an incompressible and inviscid flow that density remains constant and no turbulence occurs. Without density variation, the energy equation has no link with other equations, the flow field can be solved by only considering continuity equation and momentum equations. Moreover, the viscous term can be discarded for an inviscid flow.

2.2 Numerical Models

This program divides the computation domain into a number of control volumes based on a finite volume method (FVM). For the discretization of governing equations, 1st-order and 2nd-order schemes are introduced for the transient term, upwind and central differencing are proposed for the convection term. The discretization methods result in a set of linear algebraic equations which must be solved. This program uses a AMG (Algebraic Multigrid) linear solver to solve the system of algebraic equations iteratively.

The variables are stored in a collocated arrangement. Flow equations are solved by a SIMPLE algorithm that links continuity and momentum equations by a predictor-corrector approach.

The free-surface in water-impact problems is modelled using a VOF method that regards water and air as two independent phases. In the VOF method, a transport equation has to be considered for a volume fraction α_i that represents the filled fraction of i -th phase in one control volume. High-Resolution Interface Capturing (HRIC) scheme is specifically made for modeling the convective transport of immiscible fluid components and tracking the sharp free surface. Current study shows that a high grid resolution is very important to solve the transport equation and capture an exact free-surface.

Chapter 3 Slosh Problem

Computation cost is one of the main restrictions for CFD analysis. Especially for violent water-impact problems, large number of time segments and high grid resolution limit an accurate CFD prediction. Thus, designing an efficient adaptive-mesh model that shows reasonable performance and saves computation cost became the first motivation of current study. Analysis was performed on a sloshing problem. Sensitivity study was also carried out on the numerical parameters, e.g. spatial discretization and time difference. CFD computation presented large flow deformation and strong impact load in this study, showing reasonable agreement with that of experiment measurement.

3.1 Computational Model

A two-dimensional rectangular tank with the dimension of 630.7 mm (L) \times 446.7 mm (H) was built in CFD program, as shown in Fig. 3.1. Tank filling ratio is 0.85. The reference frame is attached to the bottom center of the tank, and a roll motion of tank is excited around the bottom center. A field of view is fixed around the right top corner, where four probe points are prepared to extract impact pressures. The probe points are regularly distributed with a space of 11.1 mm between two centers, and the first point is 3.4 mm from the right sidewall. Detailed geometry can be found in Fig. 3.1.

Eq. 3.1 represents the motion of equation (Loysel *et al.*, 2013) that excites the roll motion of tank. The motion amplitude θ_A is 4.5 degree, excitation frequency ω/ω_n is

1.0752 and simulation time T_{total} is 1.4 second. The partial-filled tank rotates and generates one wet-drop-type impact, in which the free-surface hits the tank top without trapped air. Fig. 3.2 shows sequential snapshots of instantaneous free-surface shapes for the impact at right tank ceiling.

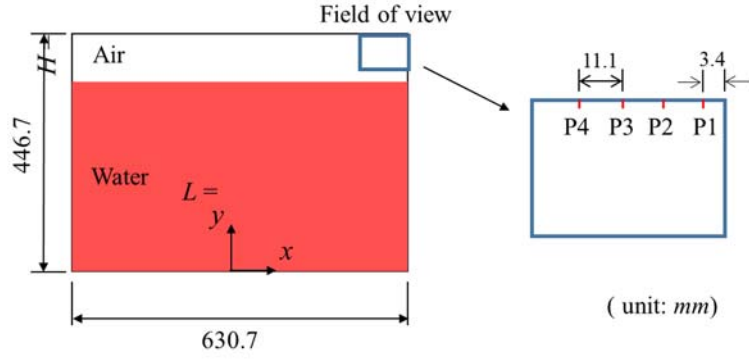


Fig. 3.1 Schematic view of tank and probe points

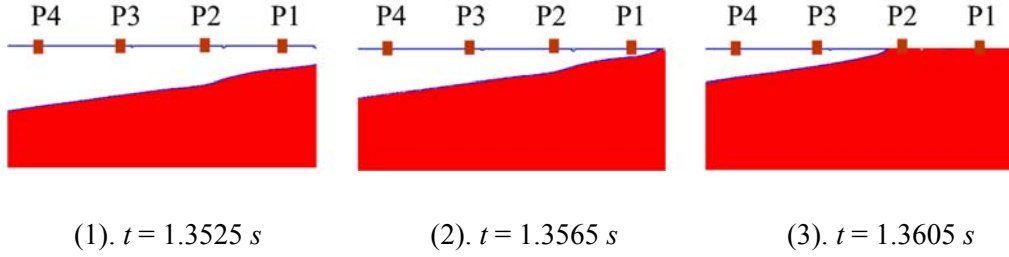


Fig. 3.2 Snapshots of free surface shapes during impact

$$\theta(t) = \begin{cases} \theta_A \tanh\left(\pi \frac{t^2}{T}\right) \sin\left(2\pi \frac{t}{T}\right) & \text{if } t \leq T \\ \theta_A \tanh\left(\pi \frac{(2T-t)^2}{T}\right) \sin\left(2\pi \frac{t}{T}\right) & \text{if } T \leq t \leq 2T \end{cases} \quad (3.1)$$

3.2 Parametric Sensitivity Study

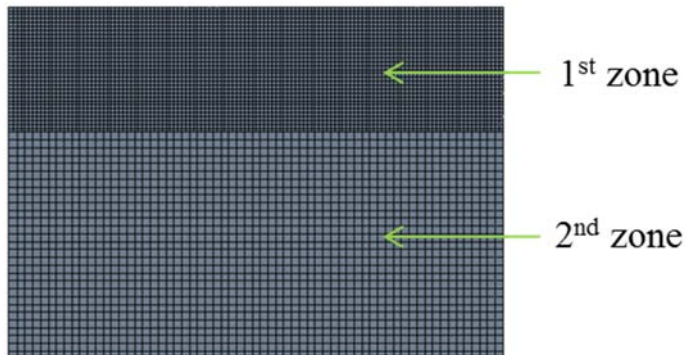
3.2.1 Solution Grids: Adaptive Meshes

Adaptive mesh model with trimmed cells is used in current study. A small area of fine mesh is constructed around the impact region, while relatively coarse grids are used for the rest place. Two factors are concerned for adaptive refinements: the size of refinement area and refinement degree. Correspondingly, three types of mesh models have been designed and presented in Fig. 3.3. The model is divided into multiple zones and Δx_{min} denotes the minimum grid size of one model. For each model, the grid size is set to be Δx_{min} in the 1st zone and then be enlarged to $2\Delta x_{min}$ and $4\Delta x_{min}$ in the 2nd and 3rd zones respectively.

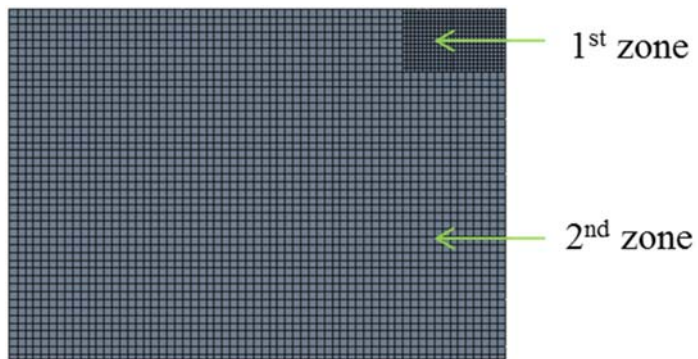
The comparison idea is to use the same value of Δx_{min} for each type of mesh, and then compare the impact pressure, free-surface development and CPU computation time. Three sets of comparison have been performed using different $L/\Delta x_{min}$ values: 400, 800 and 1200. Table 3.1 summarizes the number of grids that are required for each mesh model. It is worth noting that type 3 significantly reduces the number of grid comparing with other two types.

Table 3.1 Number of grids for mesh models with different $L/\Delta x_{min}$ (unit: million)

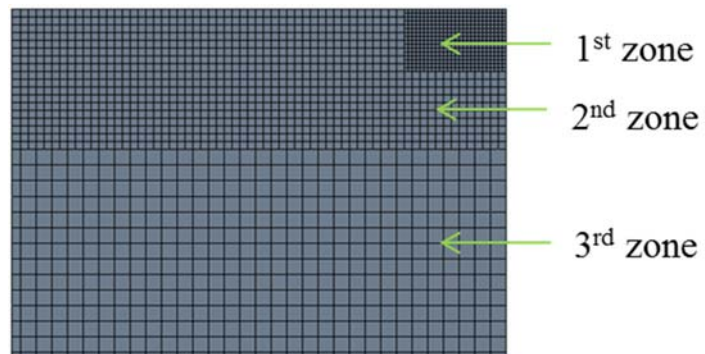
$L/\Delta x_{min}$	400	800	1200
Type 1	0.057	0.228	0.509
Type 2	0.031	0.124	0.277
Type 3	<u>0.017</u>	<u>0.067</u>	<u>0.149</u>



(1). Type 1



(2). Type 2



(3). Type 3

Fig. 3.3 Three types of adaptive mesh models

Comparison was firstly observed on pressure signals that are recorded from point 2 and point 4, as shown in Fig. 3.4. Higher grid resolution produces smoother signals and larger peak values. Meanwhile, Fig. 3.4 shows a discrepancy of pressure rise instant between different mesh models, and the discrepancy is reduced as the improvement of grid resolution. This is because the instant that flow impacts the same point can be different by changing mesh model, as shown in Fig. 3.5. The difference is interpreted as a numerical error from solving the transport equation of volume fraction, and the numerical error becomes smaller when finer mesh model is applied.

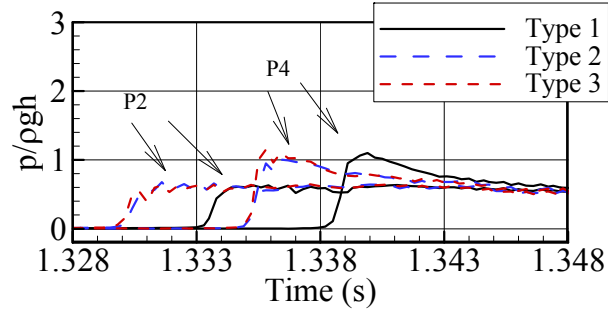
All parallel computations were performed using 8 cores, and main specifications of processor are listed in Table 3.2. From Table 3.3, model of type 3 is the one that saves CPU computation time significantly comparing with other two types. Therefore, type 3 is selected for future studies.

Table 3.2 Main specifications of processor

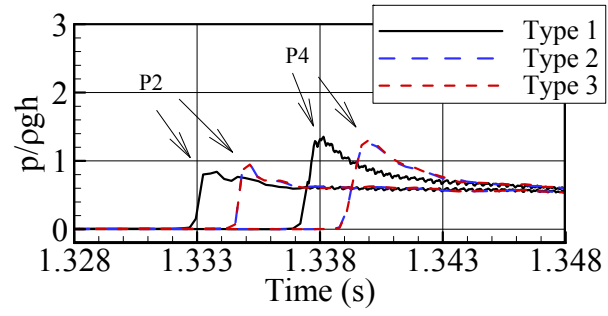
CPU	Intel Xeon CPU E3-1220 U2
Processor Base Frequency	3.1GHz
Memory Size	8 GB

Table 3.3 Computational time for each mesh model (unit: hour)

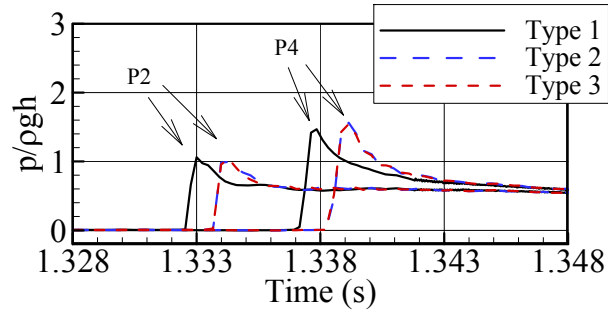
$L/\Delta x_{min}$	400	800	1200
Type 1	2.5	12.4	42.3
Type 2	1.7	7.5	24.5
Type 3	<u>1.4</u>	<u>5.0</u>	<u>13.9</u>



(1). $L/\Delta x_{min}$: 400



(2). $L/\Delta x_{min}$: 800



(3). $L/\Delta x_{min}$: 1200

Fig. 3.4 Comparison of pressure signals

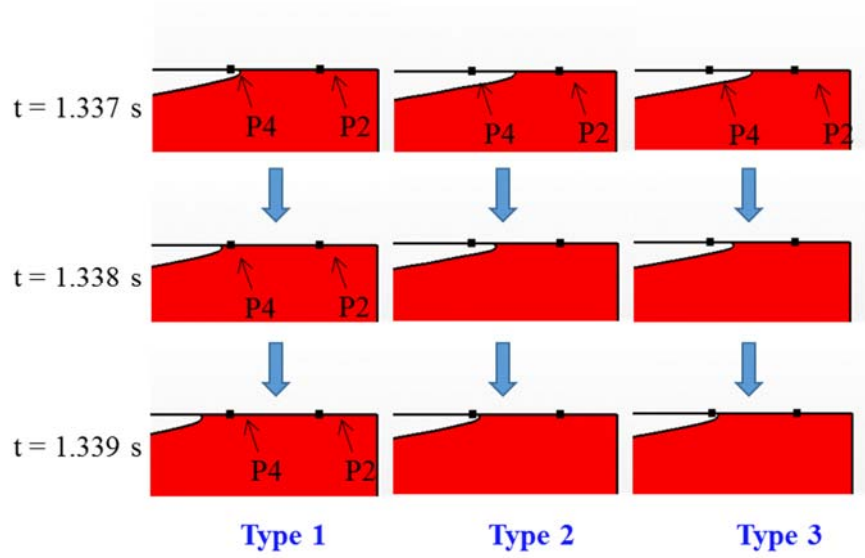


Fig. 3.5 Sequential snapshots of free-surface development at right tank ceiling

3.2.2 Sensitivity to Spatial Discretization

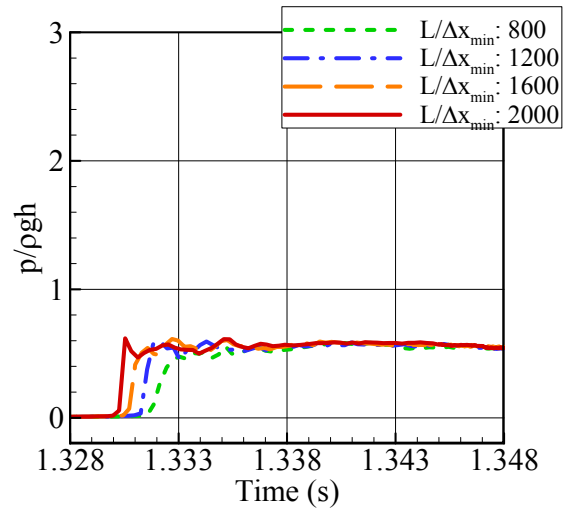
To accurately evaluate pressure field and free-surface shapes, the grid resolution must be improved and the convergence of pressure signal is expected. However, when changing the grid size, time step should be changed accordingly due to the CFL condition. CFL number involves both grid size Δx and time step Δt , and determines the stability of numerical solution, as shown below:

$$\text{CFL} = \frac{v \cdot \Delta t}{\Delta x} \quad (3.2)$$

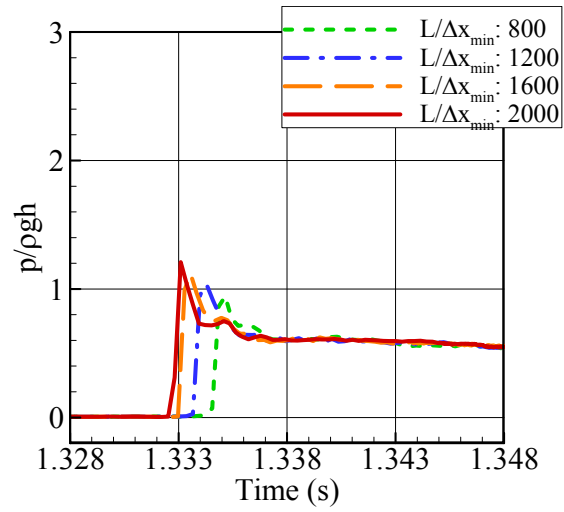
The $v \cdot \Delta t$ indicates the length that flow travels by one time-step. The length should be less than grid size, or else flow might cross more than one grid in one time-step and thus introducing numerical instability. This is very important for violent

problems because of the high pressure gradient and large velocity variation. Therefore, the ratio of $\Delta t/\Delta x$ was fixed and the maximum CFL value was kept around 0.8 in this section. The sensitivity about time step will be investigated in next section.

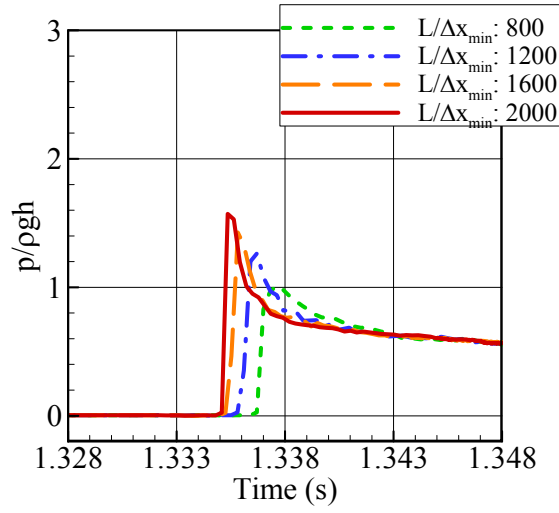
Fig. 3.6 plots the pressure signals obtained by different grid resolutions, and common characteristics can be observed on every probe point. Firstly, the signals have a tendency of higher peak values and earlier rise instants as the improvement of grid resolution. Moreover, pressure rises to peak value more rapidly using finer mesh models. Fig. 3.7 shows the change of pressure peak values over $L/\Delta x_{min}$ values. Convergence can be expected using more refinements, but it is limited by current computation capability. Therefore, a mesh model with $L/\Delta x_{min} = 2000$ has been decided for next studies.



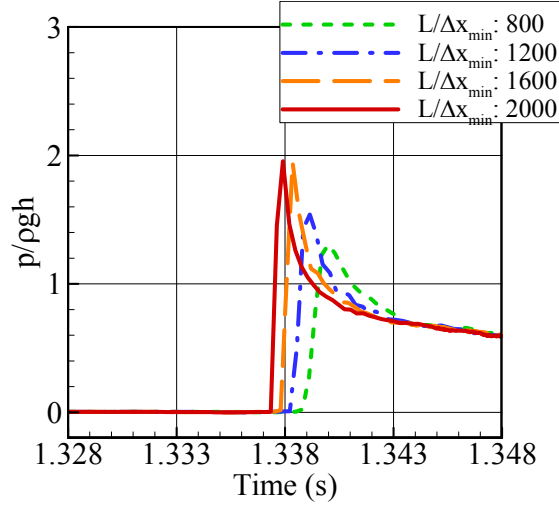
(1). Signals on point 1



(2). Signals on point 2



(3). Signals on point 1



(4). Signals on point 2

Fig. 3.6 Pressure signals on four probe points

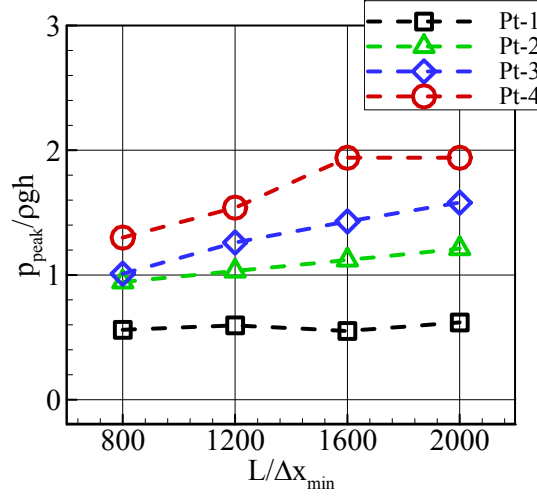
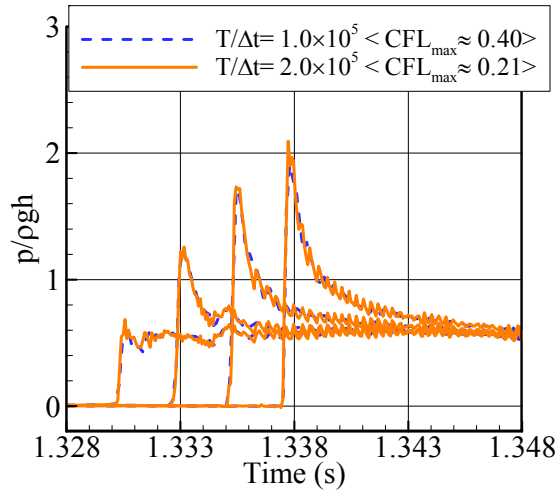
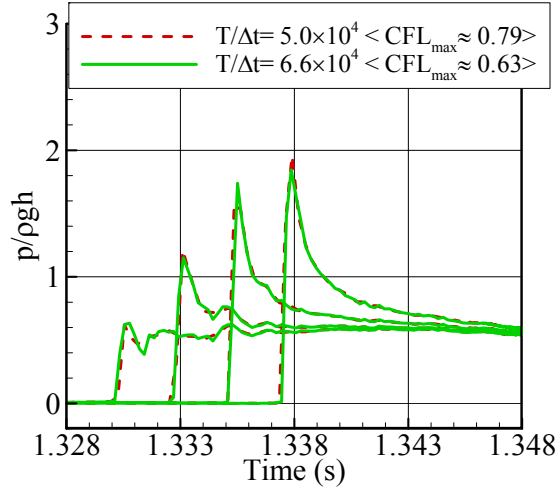


Fig. 3.7 Pressure peak values over $L/\Delta x_{\min}$

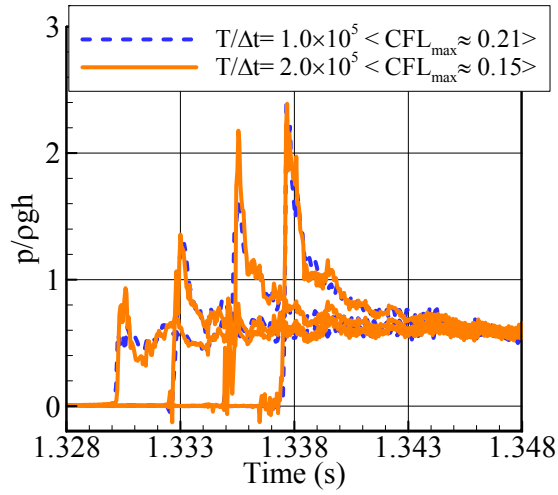
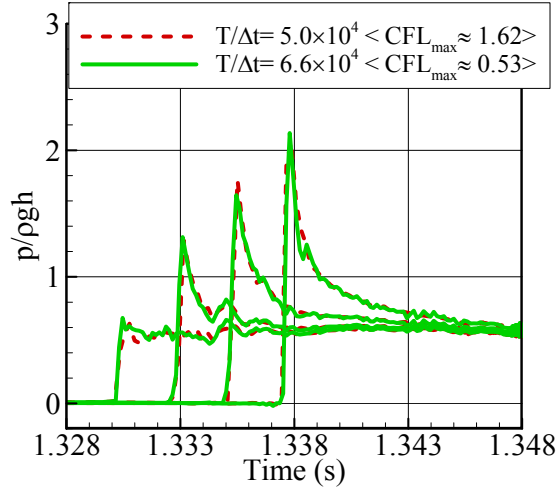
3.2.3 Sensitivity to Temporal Discretization

Current commercial program provides an implicit method for the time integration. In implicit method, the time step is fixed while CFL value fluctuates. Thus the maximum value of CFL number (CFL_{\max}) has to be observed for whole computation progress.

In the program there are two temporal schemes: 1st-order scheme and 2nd-order scheme. With each schemes, pressure signals all become oscillating when using very small time step. This might due to that time step plays a denominator role in temporal term ($\frac{d(\rho\phi V)}{dt}$), thus small time step makes this term sensitive. However, convergence of pressure peak value can be observed in Fig. 3.8. The peak pressure values tend to be higher in the case that CFL_{\max} value is less than 0.4. This is in fact the spike value of oscillation signals. As a conclusion, an appropriate time step that ensures CFL_{\max} value varies around 0.6 to 0.8 has been selected in future studies.



(1). Signals by 1st-order scheme



(2). Signals by 2nd-order scheme

Fig. 3.8 Pressure signals obtained by different temporal schemes and time steps

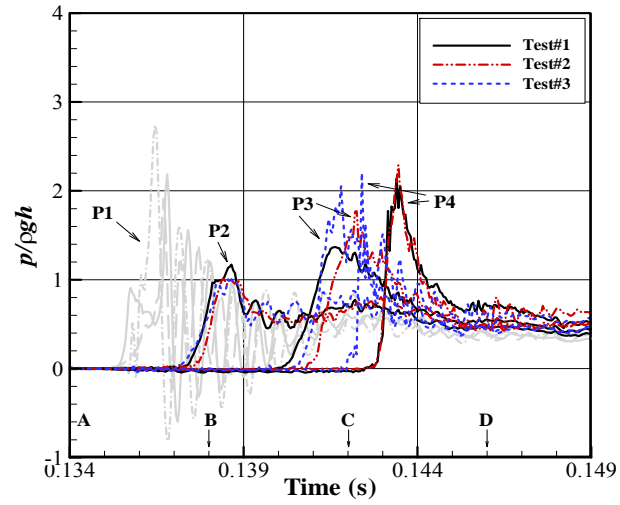
3.3 Results and Discussions

The impact characteristics were compared with that from a PIV test, which was carried out by Yang *et al.* (2015). Since the PIV system was triggered right before the impact occurred, pressure measuring system created a time axis that is different from CFD computations.

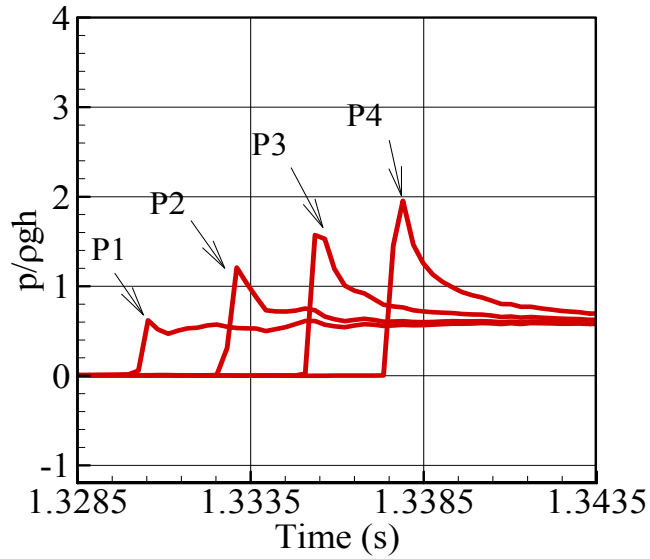
Fig. 3.9 shows the comparison of pressure signals between PIV test and CFD computations. The signals show similar trend for probe points except P1, which is located near the sidewall. In experiment, P1 recorded an extremely oscillating pressure signal that might be due to unexpectedly trapped air. More explanation on the results of PIV test can be found by Yang *et al.* (2005).

Fig. 3.10 shows the comparison about free-surface development and velocity vectors. Snapshots show that free-surface moves upwards with a vertical velocity before hitting the ceiling, and then impacts the wall and generates a jet flow to left side. Similar patterns are observed between PIV tests and CFD computations, therefore reasonable agreement has been achieved in this study.

In this chapter, main contributions were the construction of an efficient adaptive mesh model and investigation into the sensitivity of numerical parameters. Appropriate numerical conditions were decided and a reasonable agreement was arrived between CFD results and PIV measurements.

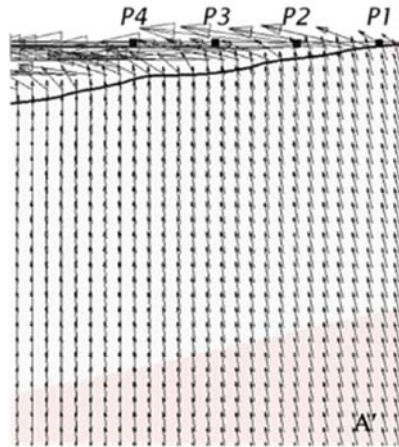
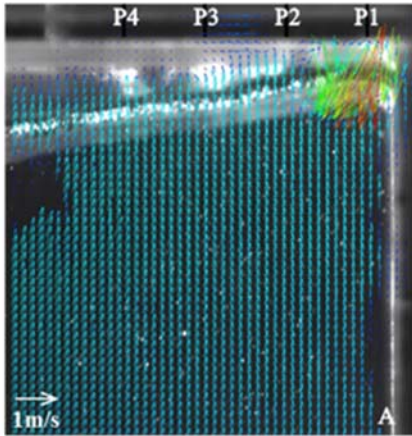


(1). Pressure signals from PIV tests

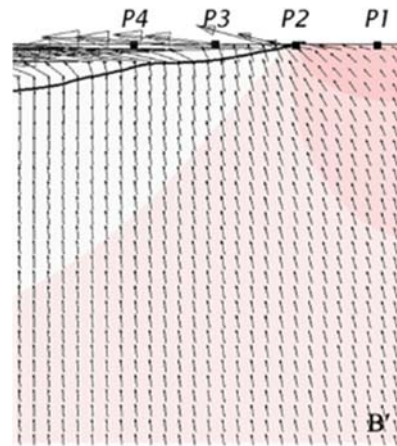
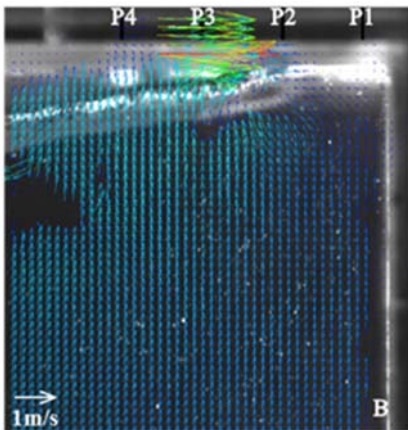


(2). Pressure signals from CFD computations

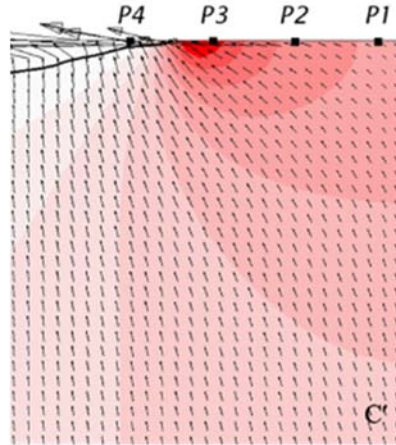
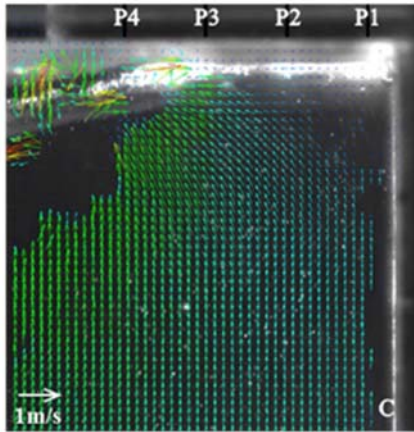
Fig. 3.9 Comparison of pressure signals between PIV test and CFD computation



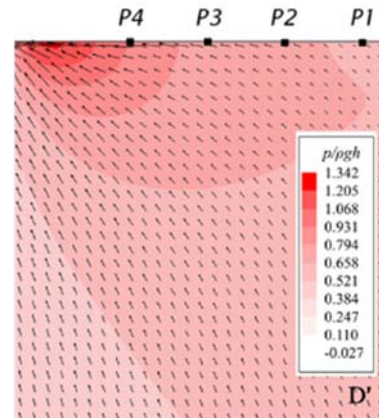
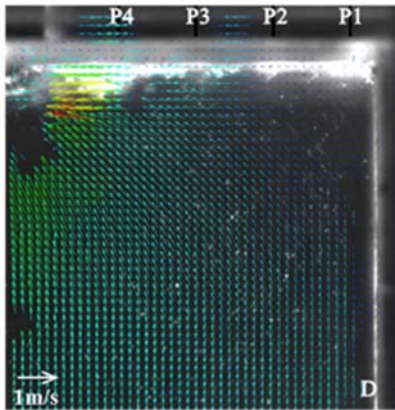
(1) A: $t = 0.134$ s and A': $t = 1.3296$ s



(2) B: $t = 0.138$ s and B': $t = 1.3336$ s



(3) C: $t = 0.142$ s and C': $t = 1.3376$ s



(4) D: $t = 0.146$ s and D': $t = 1.3416$ s

Fig. 3.10 Snapshots of free-surface development and velocity vector at right tank ceiling
(PIV tests (left) and CFD computations (right))

Chapter 4 2-D Water-Entry Problem of Wedge and Ship-Like Sections

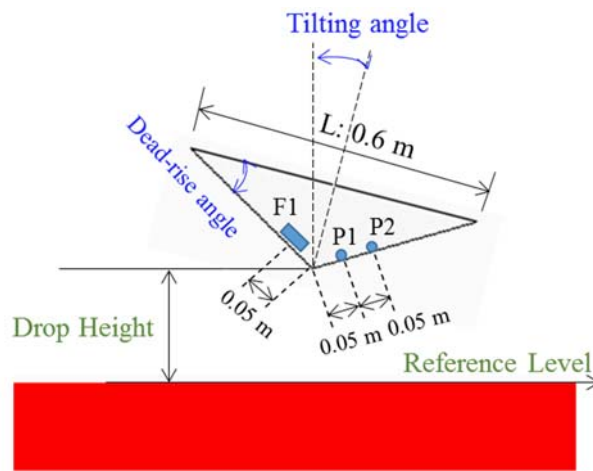
Water-entry is another common phenomenon that produces violent impacts. Potential theory has been widely used on this topic, but previous predictions are limited to simple geometry and two-dimensional condition. Therefore, applying the CFD analysis on this problem became the second study of this thesis. Numerical uncertainties that appear in CFD computations were also investigated through parametric sensitivity studies. Moreover, this problem involved an overset-mesh technique that allows a rigid body to move inside computational domain. Observing the performance of overset-mesh technique was another motivation for this study.

4.1 Computational Models

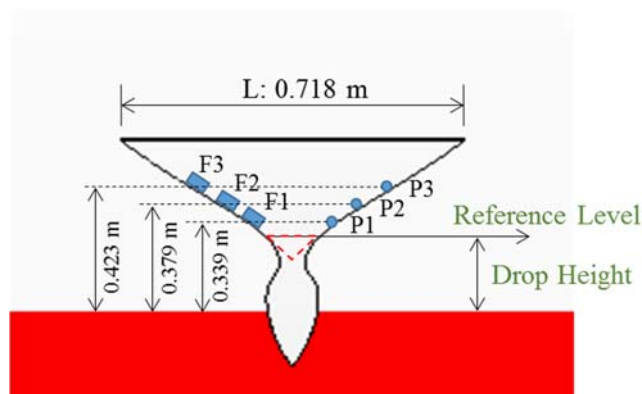
^[6]KRISO carried out a comparative study on the water-entry problems in 2014. Current study applied the same section models with that of KRISO tests, as in Fig. 4.1. Table 4.1 lists four cases with different drop conditions: the wedge section that has 30 degree of dead-rise angle was dropped by two different tilting angles, and ship section has no tilting angle but was dropped at two different heights. The first case was used for parametric sensitivity studies, and then final computation and validation were performed on all the four cases. Pressure and force sensors were arranged at section bottom for impact observation.

To simulate the free falling of sections inside computational domain, two overlapping mesh models that one only contains the rigid body and another one

contains the whole computation domain were modelled. Ship sections are modelled in 3-D condition with several layers of mesh in z direction. Fig. 4.2 shows half of the geometry with boundary conditions, the two boundary planes that are proportional to y axis are of symmetry conditions, and no air exists between these two boundaries and rigid bodies. Tests have shown that the number of grid layers in y direction has no effect on numerical results, so only one layer of grid was modelled in y direction.



(1). Wedge section



(2). Ship section

Fig. 4. 1 Geometry of two ship-like sections

Table 4. 1 Drop conditions

Case	Section	Drop height (m)	Tilting angle (deg)
#1	Wedge section	0.50	0
#2			30
#3	Ship Section	0.17	-
#4		0.30	

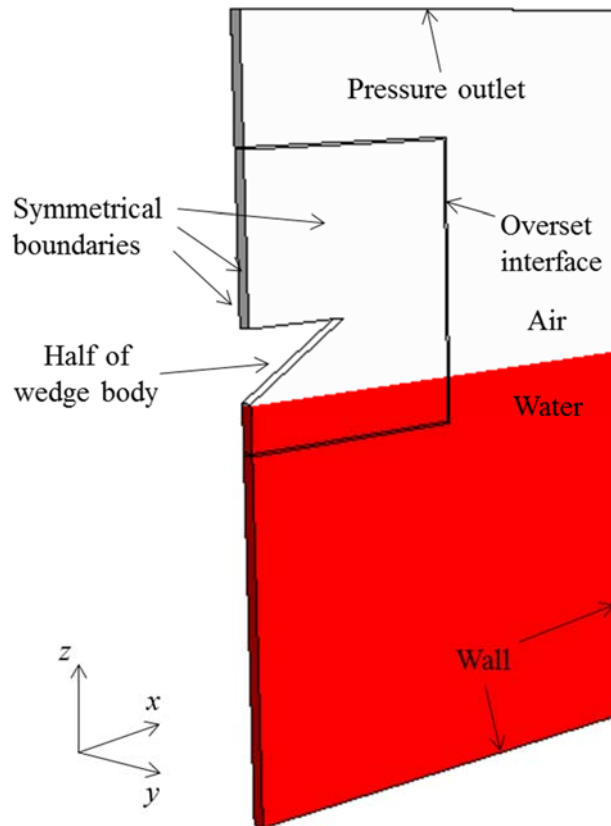


Fig. 4. 2 Computation domain (half) and boundary conditions

4.2 Parametric Sensitivity Study

4.2.1 Sensitivity to Mesh Models

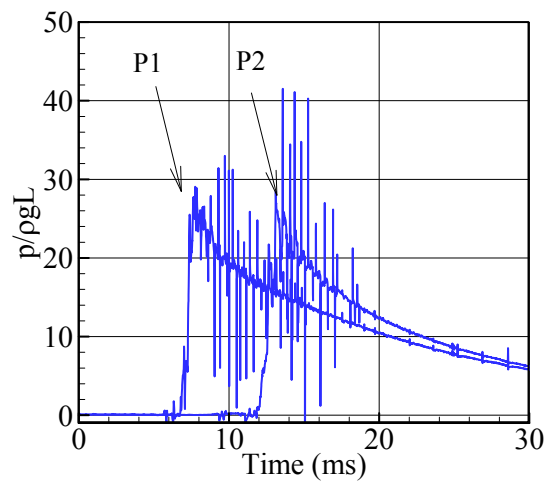
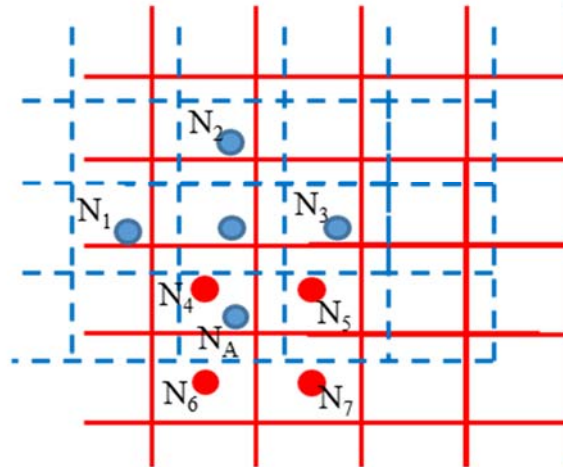
This water-entry problem involves two techniques constructing the mesh mode: overset mesh, adaptive refinement.

Overset-mesh technique allows that two overlapping meshes communicate the variables at the overset interface by interpolation method. The effects of overset region such as region size and data mapping are firstly observed. Fig. 4.3 presents two examples of data mapping. An appropriate mapping indicates that both grid size and position of grid centroid match well at the initial stage of computation, as Fig. 4.3(2). Because the free-falling motion makes overset mesh moves vertically inside background mesh, a transversal discrepancy between grid centroids of two overlapping meshes will introduce errors during the whole computation. Fig. 4.3(1) presents an extremely oscillating pressure signal that due to inappropriate data mapping.

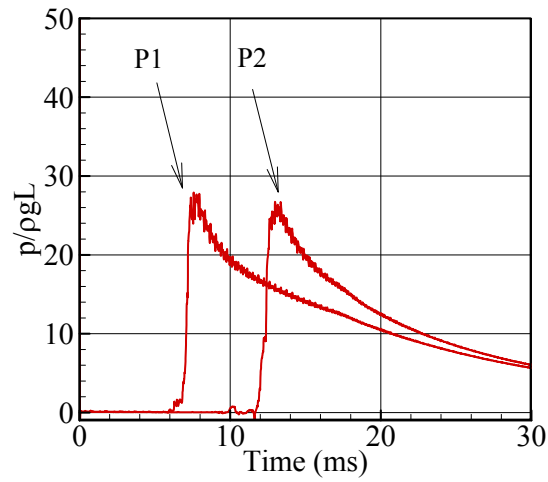
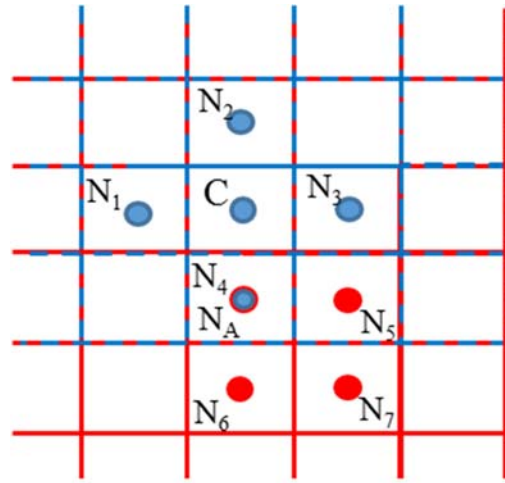
Experience from tests recommended that the size of overset region should be large enough to enclose the area of high velocity. The reason is that large variation of variables at overset interface could introduce error to the interpolation and thus break the computation.

There many interpolation methods, e.g. distance weighed method, linear method, and least squares method, available for overset interpolation. Tests had shown almost no distinction in terms of computation results.

- - - - - Overset mesh
 ——— Background mesh



(1). Inappropriate mapping and computation results



(2). Appropriate mapping and computation results

Fig. 4. 3 Two examples of data mapping at inial computation stage
(up.: arrangement of two overlapping mesh; down: pressure signals)

4.2.2 Sensitivity to Time Step

In the chapter about sloshing problem, sensitivity study of time step showed that pressure signals are nearly convergent but also become oscillating when time step is too small. Therefore, a similar behavior is expected for water-entry problem. Table 4.2 presents the four cases that use different time step. The maximum CFL number for each case is also listed in table 4.2. The grid resolution is fixed to 300, and simulation time T is 30ms.

Table 4. 2 Four computation cases with different time steps

Case	$T/\Delta t$	CFL_{\max}
#1	8.0×10^4	≈ 0.2
#2	3.0×10^4	≈ 0.4
#3	3.5×10^4	≈ 0.6
#4	2.0×10^4	≈ 0.8

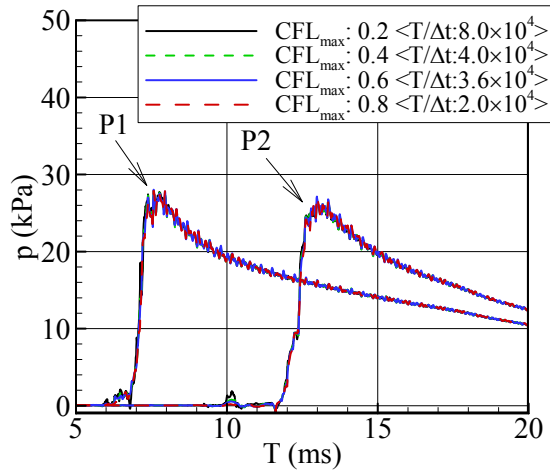


Fig. 4. 4 Pressure time signals for different cases

4.2.3 Sensitivity to Grid Size

Before the convergence test of grid size, an investigation was performed into the reason for signal oscillation. A series of trial and error have been conducted and proofed that numerical conditions, such as time step, mesh arrangement, boundary condition and multigrid solver, have no direct relationship with the oscillation. The oscillating phenomenon was caused by unexpected trapped air, which is in fact a numerical error that due to grid resolution. It can be observed in Fig. 4.6 that as grid resolution increase, the unexpected air becomes smaller and pressure signals have shorter oscillation period and relieved oscillation amplitude. So high grid resolution is very significant for this problem.

However, unlike the sloshing problem, water-entry problem used a relatively low $L/\Delta x_{min}$ value due to the larger computational domain and more refinement areas. A further refinement of grid size might be able to eliminate the oscillation but it is limited by computation cost. Thus a moving average filter with a filtering span of 45 points was applied to eliminate the oscillation, as below:

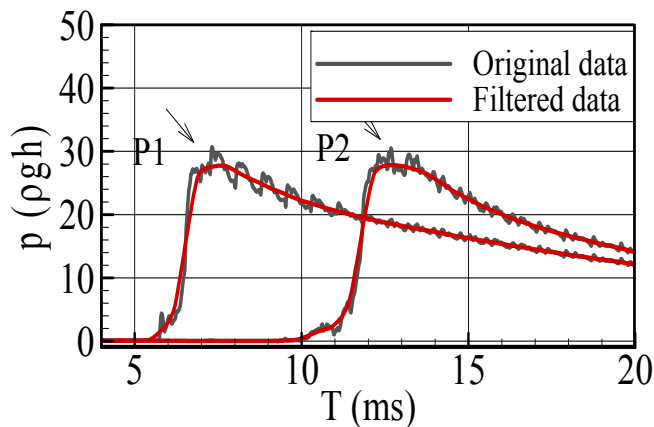
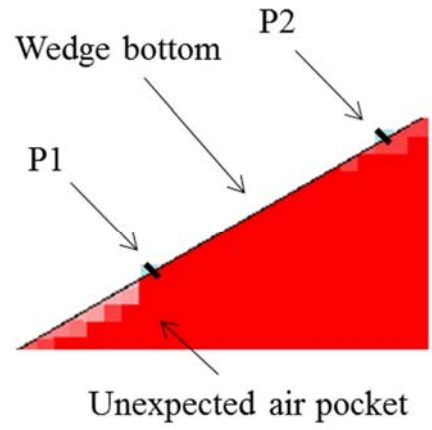
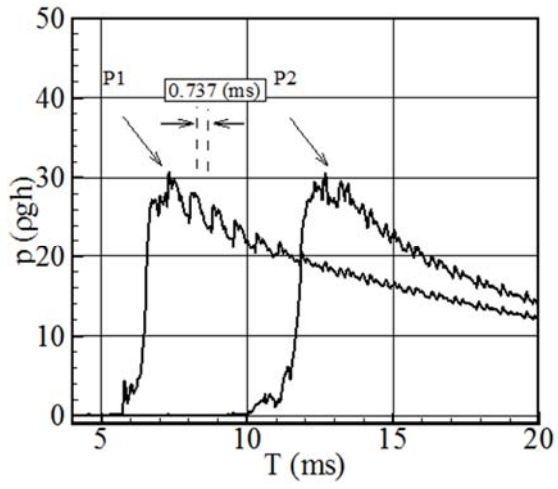
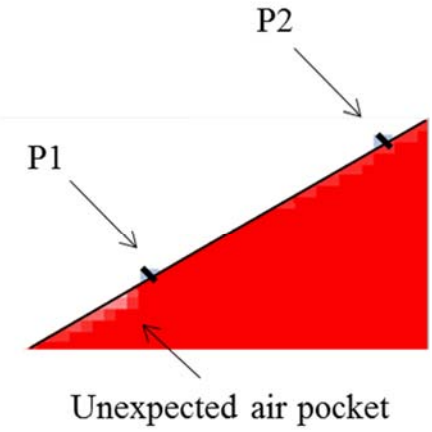
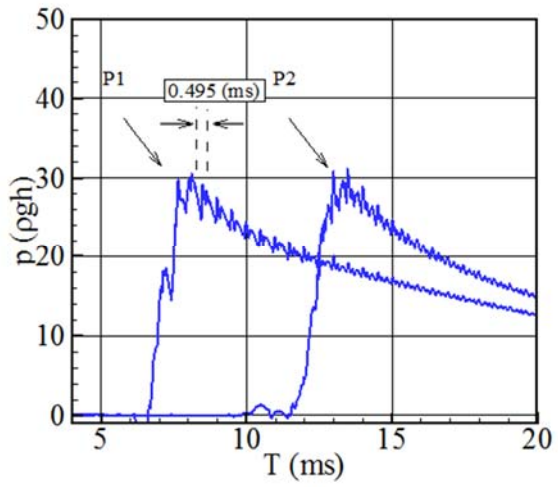


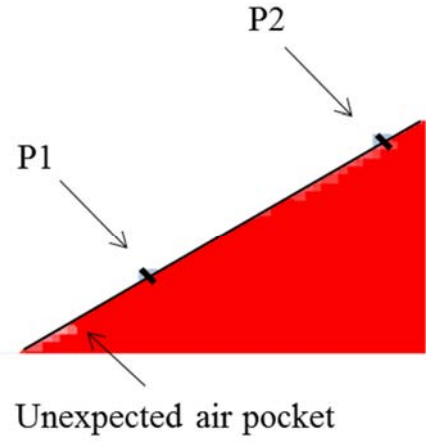
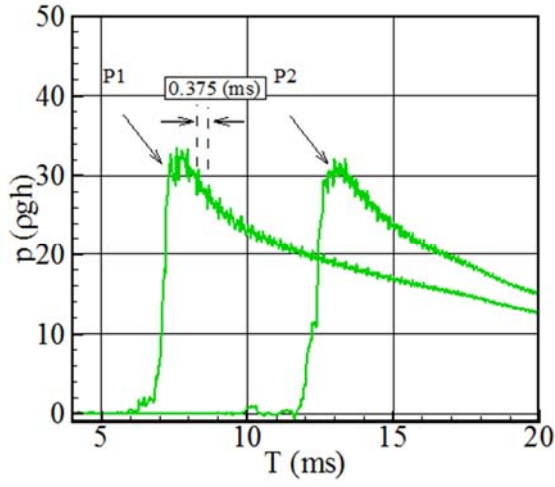
Fig. 4. 5 Comparison of original data and filtered data



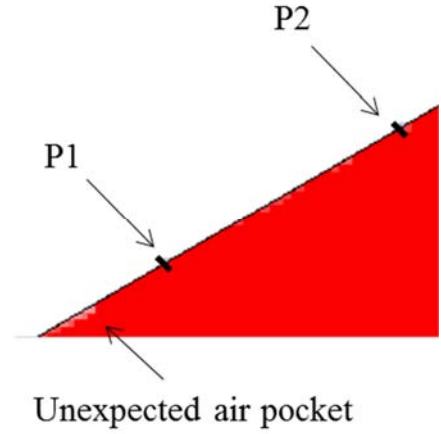
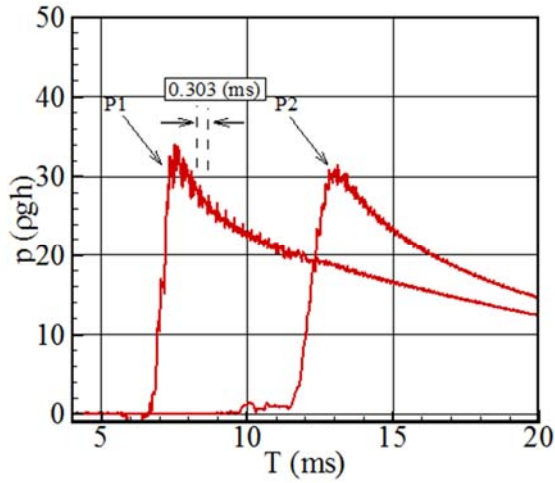
(1). $L/\Delta x_{min}$: 200



(2). $L/\Delta x_{min}$: 300



(3). $L/\Delta x_{min}$: 400



(4). $L/\Delta x_{min}$: 500

Fig. 4. 6 Results using different grid resolutions

(left: pressure signals; right: fraction distribution around wedge bottom)

Fig. 4.7 shows filtered results. A Grid Convergence Index (GCI) that proposed by

Celik *et al.* (2008) was used to estimate the convergence. The estimation starts by determining grid refinement factor with three different sets of grids. Then computing the apparent order of convergence by fixed-point iteration, and evaluating relative errors. Table 4.3 presents the estimations for current cases using three $L/\Delta x_{min}$ values: 300, 400 and 500, the numerical uncertainty in the fine-grid solution is less than 2%, which is an acceptable value. The estimation steps are summarized as following:

- Grid refinement factors:

$$r_{21} = h_2/h_1; \quad r_{32} = h_3/h_2 \quad (4.1)$$

- Apparent order:

$$p = \frac{1}{\ln(r_{21})} \left| \ln |\varepsilon_{32} / \varepsilon_{21}| + q(p) \right| \quad (4.2)$$

$$q(p) = \ln \left[(r_{21}^p - s) / (r_{32}^p - s) \right] \quad (4.3)$$

$$s = 1 \times \text{sgn}(\varepsilon_{32} / \varepsilon_{21}) \quad (4.4)$$

$$\varepsilon_{32} = \phi_3 - \phi_2, \quad \varepsilon_{21} = \phi_2 - \phi_1 \quad (4.5)$$

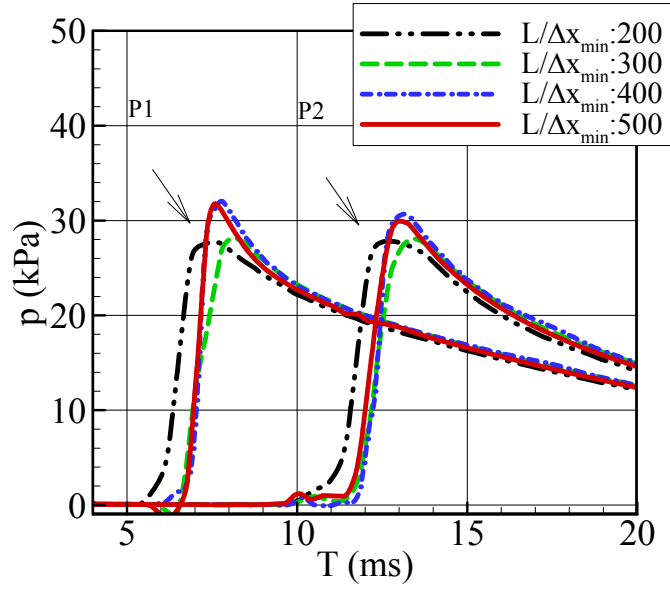
- Relative error:

$$e_a^{21} = \left| \frac{\phi_1 - \phi_2}{\phi_1} \right| \quad (4.6)$$

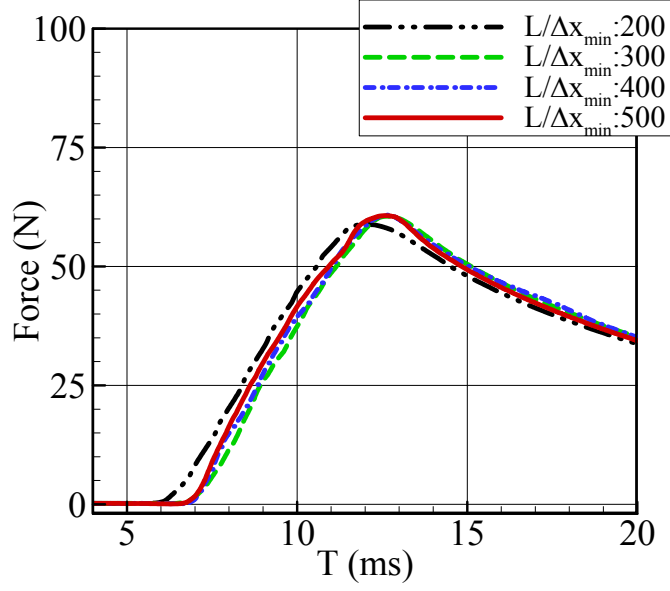
- GCI value:

$$GCI_{fine}^{21} = \frac{1.25e_a^{21}}{r_{21}^p - 1} \quad (4.7)$$

(h : minimum grid size in one mesh model; ϕ_i : peak value of variable of i -th grid)



(1). Pressure signals



(2). Force signals

Fig. 4. 7 Time signals by different grid resolutions

Table 4. 3 GCI estimations for peak values of pressure and force

Variables	P1	P2	Force
r_{21}	1.250		
r_{32}	1.332		
ϕ_1	31.792	29.952	60.70
ϕ_2	32.041	30.074	60.793
ϕ_3	28.223	28.090	60.561
p	9.649	9.911	3.489
e_a	0.008	0.004	0.001
GCI (%)	0.129	0.062	0.157

4.3 Results and Discussions

As stated in section 1.2.2, many numerical solutions that based on potential theory have been developed for this water-entry problem. To simplify the problem, most of the methods followed an assumption of high Froude number (Fn) condition. Thus, numerical performance of CFD analysis in high Fn condition was observed before the comparison with potential method

Table 4.4 lists four cases with different Fn conditions. The velocity of rigid body is specified to be constant. Since that gravity effect could be negligible in high Fn condition, cases that use zero gravity acceleration (g) were also calculated. Fig. 4.8 shows the non-dimensional pressure signals by using different values of Fn and g . Only the conditions that g is 9.81 and Fn is less than 1.0 produced different signals, all others yield similar signals. The reason is that dynamics pressure ($0.5\rho v^2$)

dominants in high Fn condition while static pressure (ρgh) plays a more important role in low Fn condition.

Table 4. 4 Four cases with different Fn conditions

Case	* Fn numbers	Constant entry-velocity (m/s)
#1	0.1	-0.2426
#2	0.2	-0.4852
#3	1.0	-2.426
#4	10.0	-24.26

* $Fn = v / \sqrt{gL}$, $L = 0.6m$

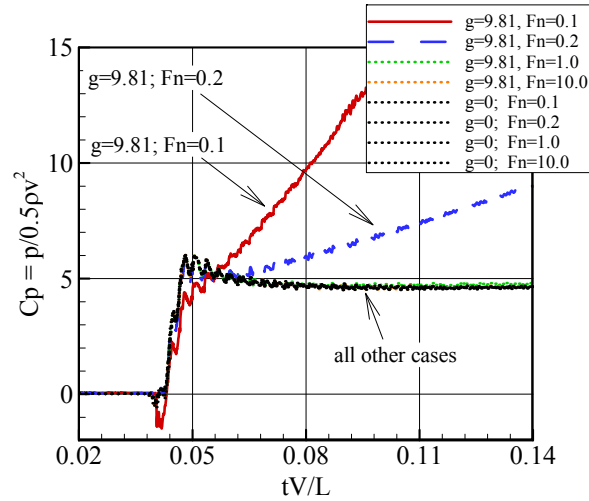


Fig. 4. 8 Pressure signals on P1

Fig. 4.9 shows the pressure distribution on wedge bottom and free-surface shapes at three instants, and good agreement has been arrived for the different conditions. Therefore, this sensitivity study showed that CFD tool performs well in high Fn condition and is able to compare with the analytical solutions.

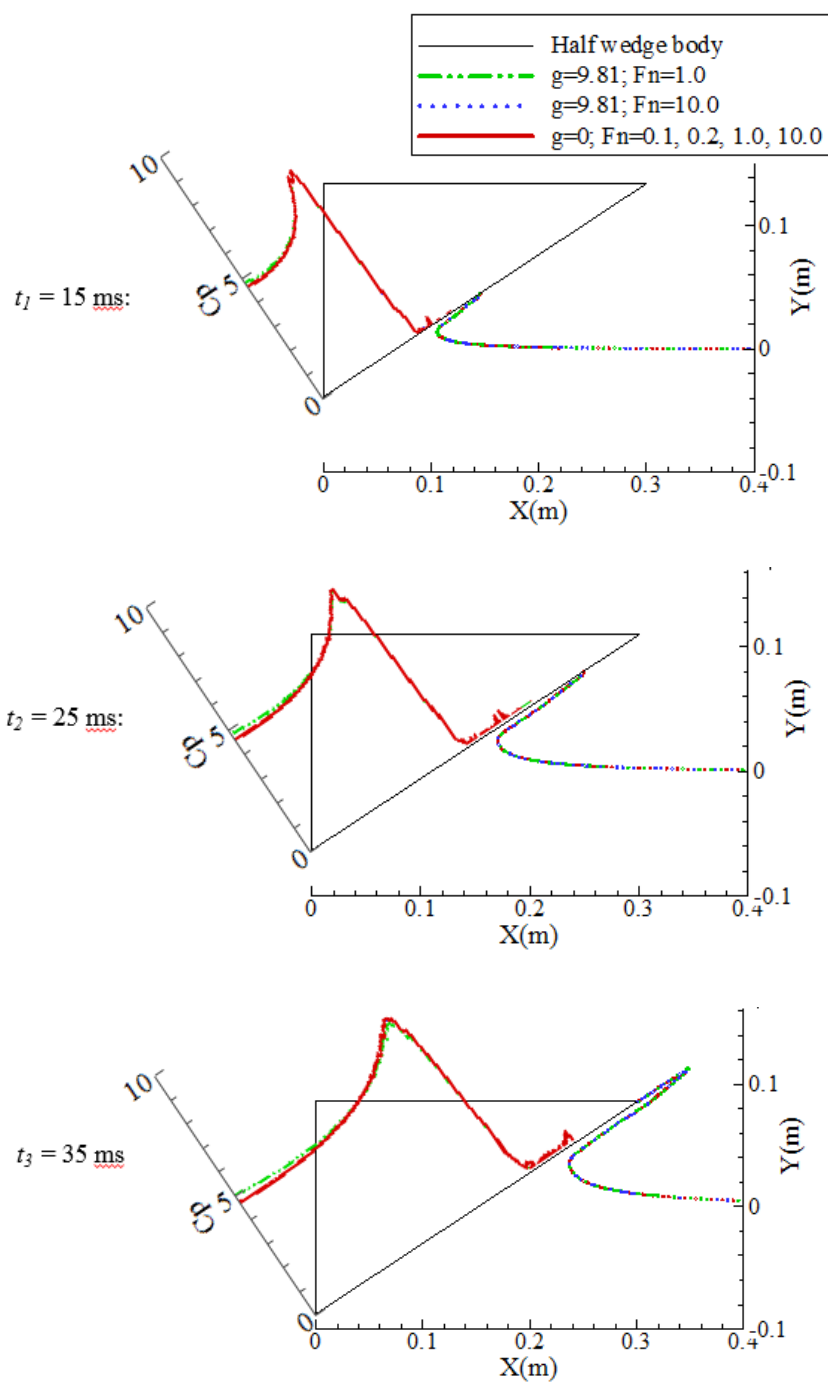


Fig. 4. 9 Pressure distribution on wedge bottom and free-surface shapes at three t

Finally, results about impact loads and free-surface shapes were observed and compared with other solutions that are introduced below. For the impact loads on ship sections, only CFD predictions and experiment measurements have been compared due to the geometric non-linearity.

- **Overset-mesh**: The present CFD computation by using overset-mesh technique
- **CIP**: A constrained interpolation profile (CIP) based CFD method and calculated by Yang *et al.* (2016).
- **GWM, MLM**: Generalized Wagner model (GWM) and modified Logvinovich model (MLM) that were proposed by Korobkin (2014) and were calculated by Yang *et al.* (2016).
- **Wagner, von Karman**: Solutions based on von Karman' and Wagner's theories

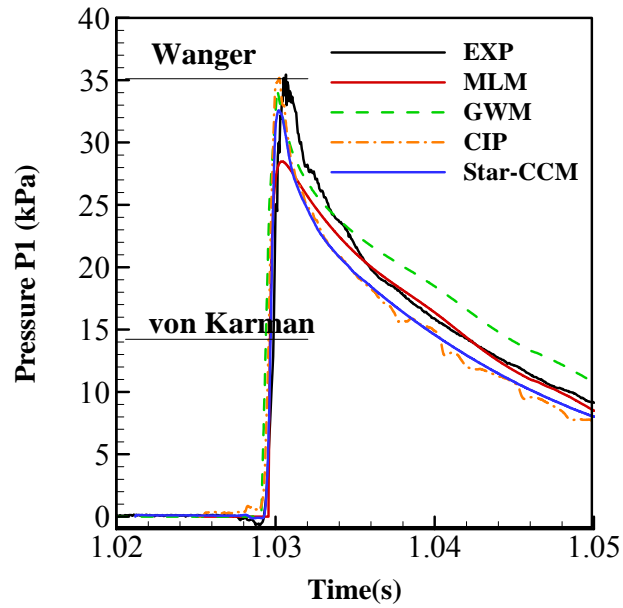
Fig. 4.10 and Fig. 4.11 presents the results for the #1 case (wedge section, tilting angle: 0). For “P1”, “overset-mesh” method yielded similar peak values and rise time with other method except MLM solution. Because ^[4]the MLM does not take into account the exact body geometry, it usually gives smaller peak pressure than the GWM when the dead-rise angle of wedge is larger than 20°. However, the pressure signals on “P2” show discrepancy in different methods. “Overset-mesh” method predicted slightly larger peak values than that of GWM and CIP methods. Fig. 4.11 is the comparison of free-surface development and pressure distribution is also presented in CFD snapshots. It shows similar shapes between “overset-mesh” method and experiment. Moreover, a jet flow that attaches at wedge bottom is obviously found in CFD snapshots.

Fig. 4.12 and Fig. 4.13 are the results of the #2 case (wedge section, tilting angle: 30°). Generally, present CFD computation show similar trends with that of CIP method. Whereas experiment measurements provided relatively low peak value, which might due to the accuracy of sensor facilities. The signals that obtained by potential methods (GWM and MLM) show overall large values. Similar patterns of free-surface evaluations are shown in Fig. 4.13.

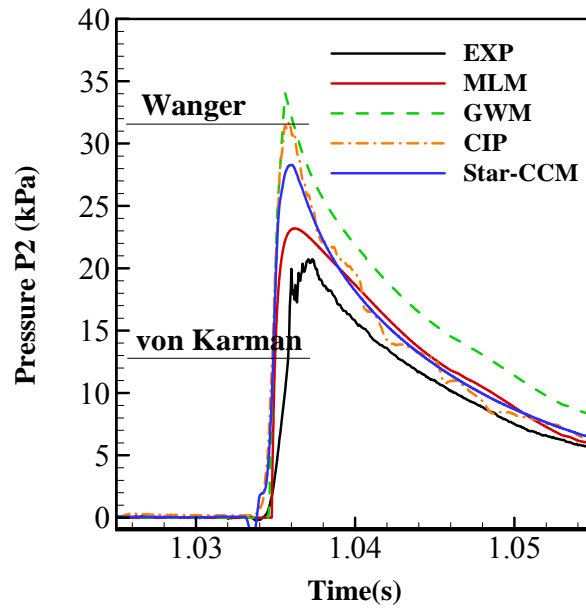
As to the impact load on ship section, three methods (current CFD computation, CIP method, experiment tests) shows common discrepancy for both the #3 case (ship section, drop height: 0.17m) and the #4 case (ship section, drop height: 0.30m). The common discrepancy is that “overset-mesh” method and CIP method produced very similar signals, whereas experiment provided signals that have relatively low peak values and longer rise time. This is shown in Fig. 4.14 and Fig. 4.16.

Sequential snapshots of free-surface are also compared in Fig. 4.15 and Fig. 4.17. Split water that detaches from body surface can be obviously found in CFD snapshots. Moreover, due to the geometric shape, similar air pocket is observed in both CFD and experiment and occurs at almost the same location. The comparison of free-surface shapes shows reasonable agreement.

Generally, present CFD computation showed acceptable predictions on the pressure behavior and free-surface development. The current numerical model can be extent to the prediction of impact loads on a more complicated geometry.



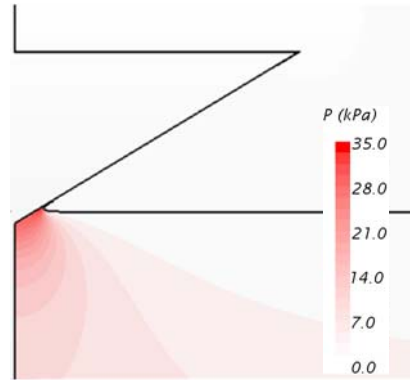
(1). Pressure signals on P1



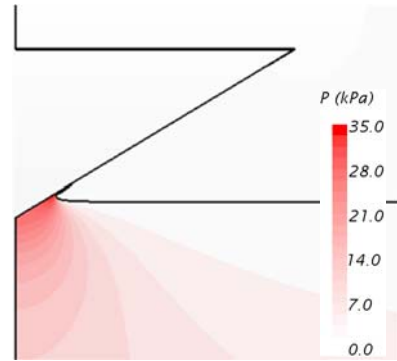
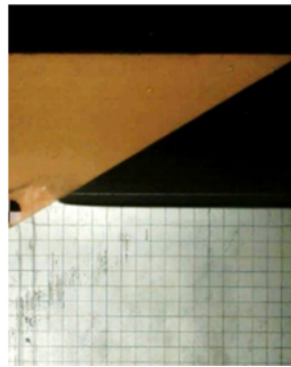
(2). Pressure signals on P2

Fig. 4. 10 Comparison of time signals (wedge section, tilting angle: 0)

$t_1 = 4 \text{ ms}$



$t_2 = 6 \text{ ms}$



$t_3 = 8 \text{ ms}$

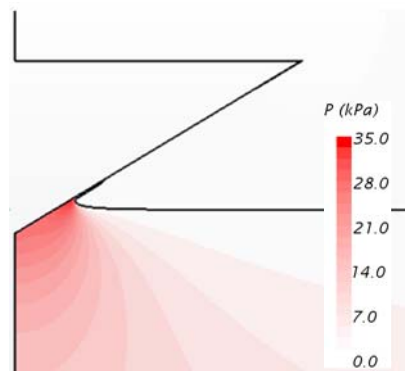
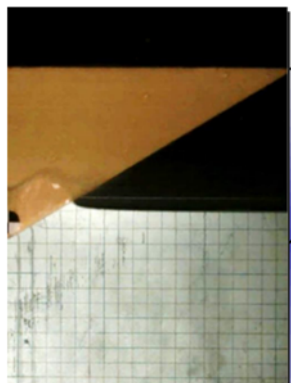
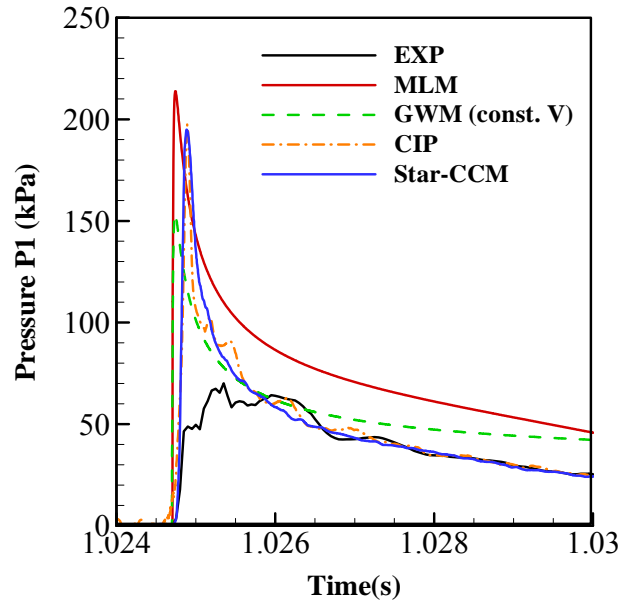
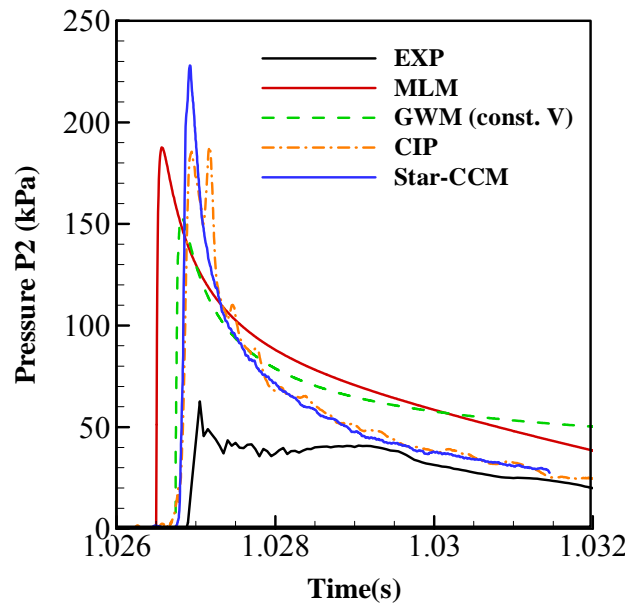


Fig. 4. 11 Comparison of free-surface shapes (wedge section, tilting angle: 0)
($t=0$ indicates the instant the body touches water)



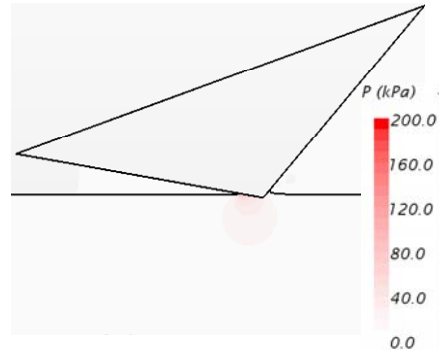
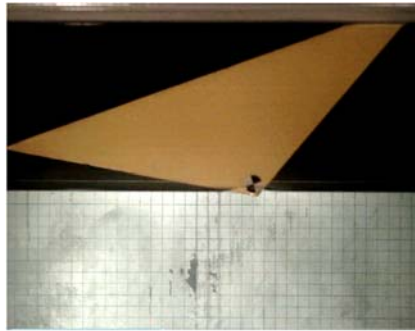
(1). Pressure signals on P1



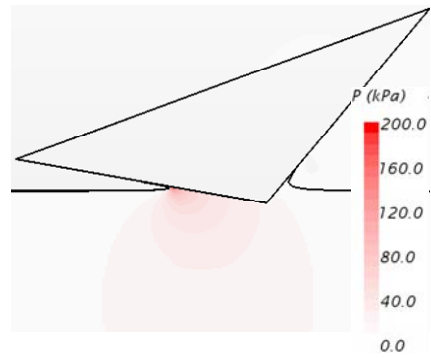
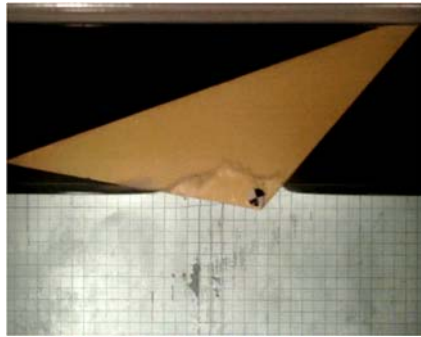
(2). Pressure signals on P2

Fig. 4. 12 Comparison of time signals (wedge section, tilting angle: 30°)

$t_1 = 4 \text{ ms}$



$t_2 = 8 \text{ ms}$



$t_3 = 12 \text{ ms}$

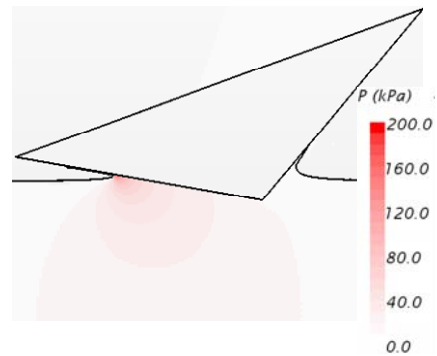
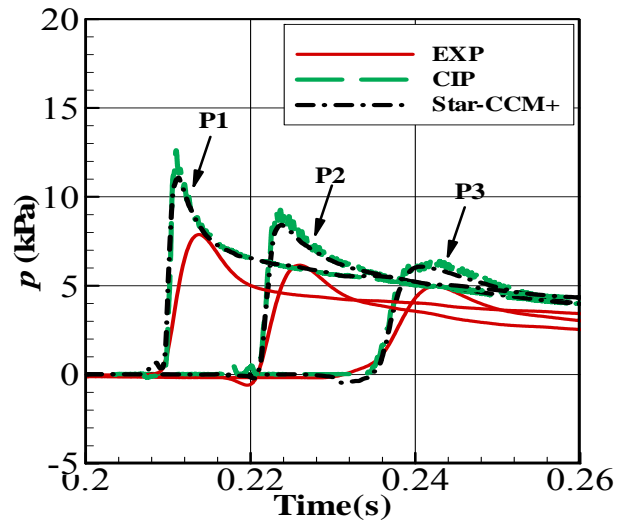
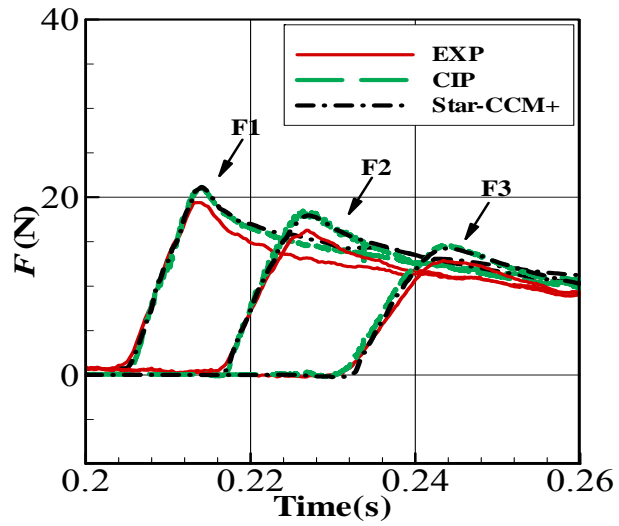


Fig. 4. 13 Comparison of free-surface shapes (wedge section, tilting angle: 30°)
($t=0$ indicates the instant the body touches water)



(1). Pressure signals



(2). Force signals

Fig. 4. 14 Comparison of time signals (ship section, drop height: 0.17m)

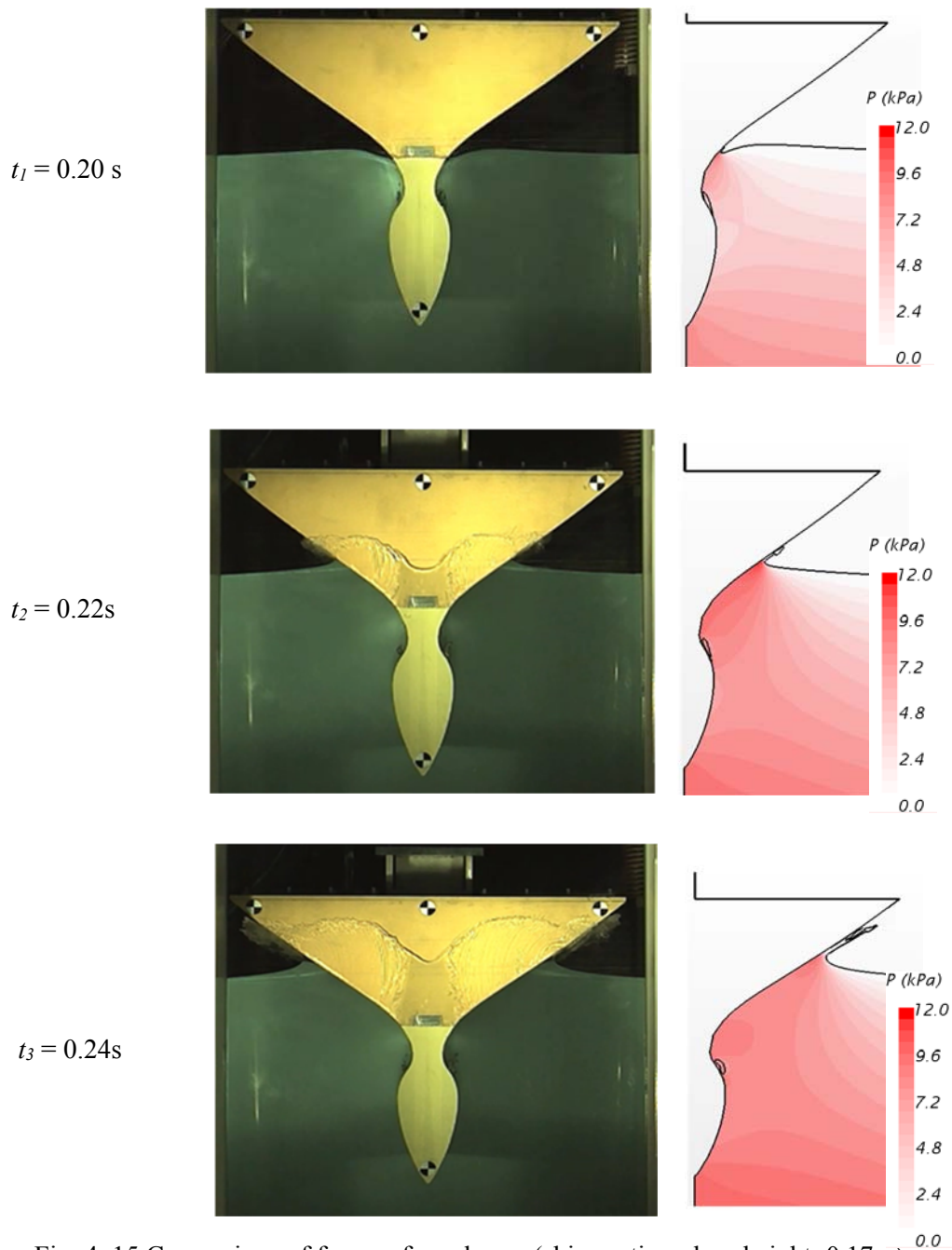
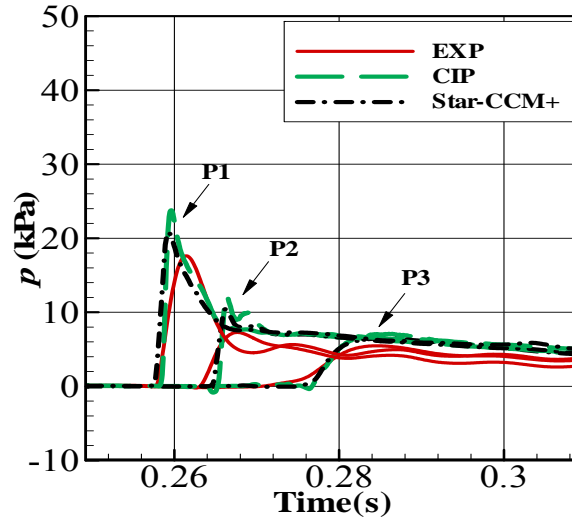
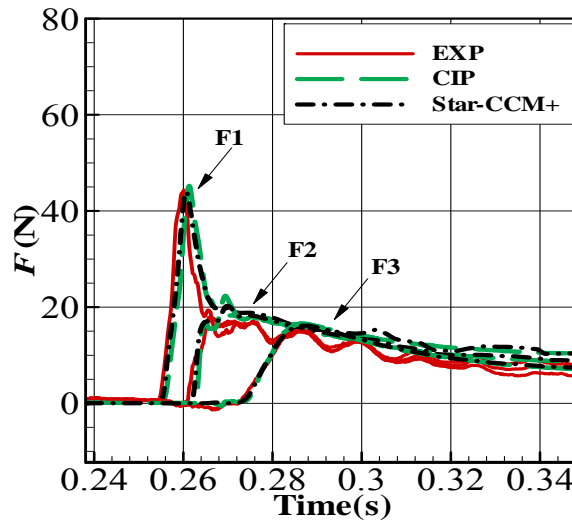


Fig. 4. 15 Comparison of free-surface shapes (ship section, drop height: 0.17m)

($t=0$ indicates start of free falling motion)



(1). Pressure signals



(2). Force signals

Fig. 4. 16 Comparison of time signals (ship section, drop height: 0.30m)

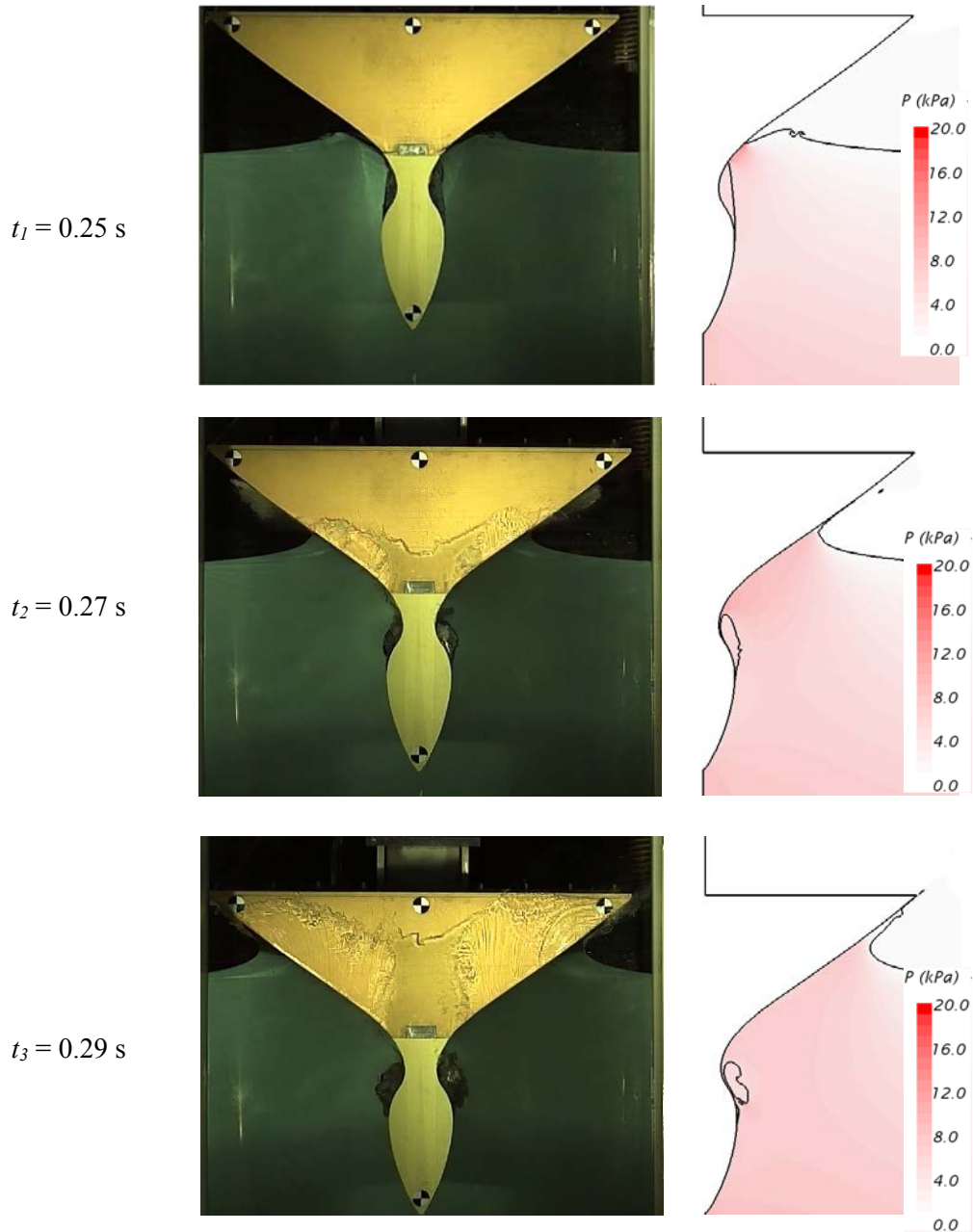


Fig. 4. 17 Comparison of free-surface shapes (ship section, drop height: 0.30m)

($t=0$ indicates start of free falling motion)

Chapter 5 3-D Water-Entry Problem of a 3D Modified Wigley

To extend the work of previous chapter to a three-dimensional case, this chapter investigated the slamming characteristics of a modified Wigley hull. Due to the limit of computation capability, parametric sensitivity study was not performed and previous experience were used to decide appropriate parameters. By comparison with the experiment data and numerical solution that integrates solution of 2-D sections along the hull length in a strip sense. The reasonable agreement proved the possibility of applying CFD analysis in real ship models.

5.1 Model Introduction

In this study, a modified Wigley with $CB = 0.56$ was dropped at specified heights and time signals about impact pressure and body acceleration were observed. The hull configuration is shown in Fig. 5.1 and can be ^[2]mathematically described as Eq. 5.1. Table 5.1 lists the main particulars of the hull.

The hull is symmetry about $x-z$ and $y-z$ planes, so only a quarter of the body was modelled in CFD program. Fig. 5.2 presents the mesh around hull, and mesh refinement is also performed at the top of ship bow because of the shape geometry. However, due to the large number of both grid and time steps, one parallel computation that utilizes 8 cores runs almost one week to simulate 0.015 s physical time. A systematical test of parametric sensitivity seems not practical, thus experience from previous chapters were utilized for the decision of appropriate

parameters. Table 5.2 lists the main parameters.

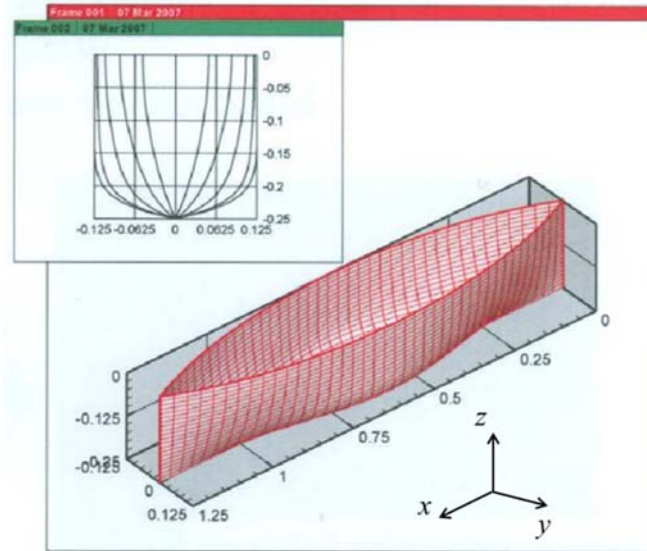
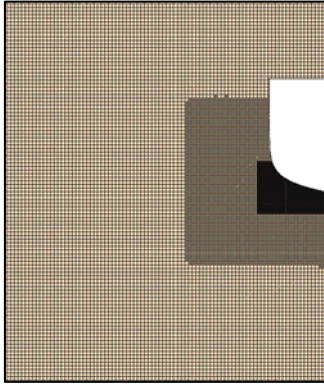


Fig. 5. 1 Configuration of modified Wigley

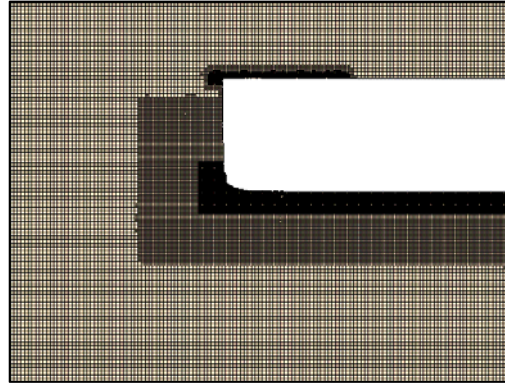
$$\left\{ \begin{array}{l} \eta = (1 - \xi^2)(1 - \zeta^2)(1 + 0.2\xi^2) + \zeta^2(1 - \zeta^8)(1 - \xi^2)^4 \\ \xi = \frac{2x}{L}, \quad \eta = \frac{2y}{B}, \quad \zeta = \frac{z}{D} \\ -L/2 \leq x \leq L/2, \quad -D \leq z \leq 0 \end{array} \right. \quad (5.1)$$

Table 5. 1 Hull geometry

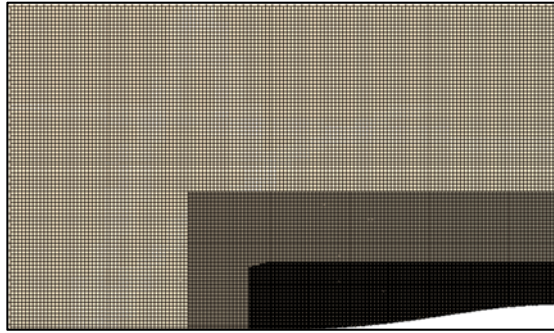
Total length (L)	1.25 m
Breadth (B)	0.25 m
Depth (D)	0.25 m
Block coefficient (CB)	0.560731
Total weight	149.44 kg·f



(1). y - z plane at $x=0.625$ m



(2). x - z plane at $y=0$



(3). x - y plane at $z=0$

Fig. 5. 2 Part of mesh model that around hull

Table 5. 2 Numerical conditions for CFD computation

Δx_{min} (m)	0.003125
Number of grids (million)	6.3
Time segment (s)	5E-6
Simulation period (s)	0.015
CFL_{max}	0.92

5.2 Results and Discussions

Fig. 5.3 presents the filtered data of body acceleration and water-impact force on hull using different drop heights. It illustrates that body experienced a large water-impact force right after entering the water, and a significant decrease can be observed in the body acceleration. It shows that higher drop height drives a more rapidly rise of impact force. Whereas peak impact force occurs at the same water-entry depth, independent of drop height, as in Fig. 5.3(c).

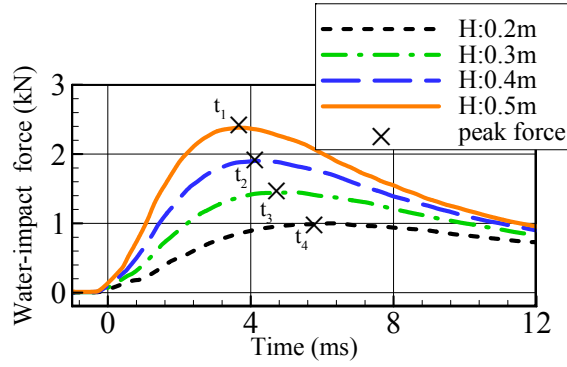
To investigate the relationship between drop height and peak impact values, some comparative results were introduced in Fig. 5.4. The experiment data was from Hong *et al.* (2012). Based on von Karman's and Wagner's theory, Hong *et al.* (2012) also approximated the cross sections of hull and calculated the sectional impact force by polynomials, and obtained the impact force on whole body by integrating along the length in a strip sense.

In Fig. 5.4, CFD results show that both the peak acceleration values and peak impact values are linearly proportional to drop height. For Fig. 5.4(1), CFD results are similar with that of experiment, but the slopes of trend line are slightly different between CFD results and experiment.

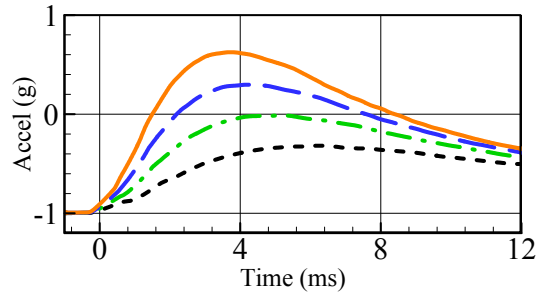
For the peak impact force in Fig. 5.4(2), Karman's solution behavior as a low bound while Wagner's solution is a high bound. CFD predictions tend to be lower than that of experiment values, but the slope of trend line is very similar.

However, due to the limit of computation capability and the strong violent free-surface during impact moment, it requires more work to further improve the grid resolution for better prediction. But current computation already showed clear

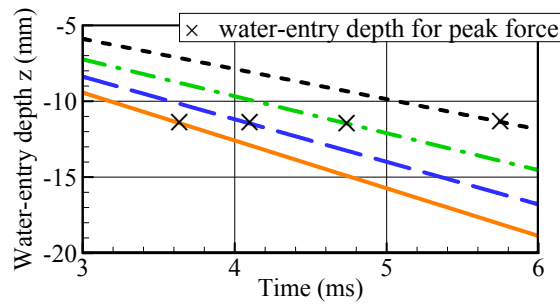
impact characteristics, such as the time signals, linearly proportional relationship between peak impact value and drop height. More explorations on 3-D cases can be expected in the future.



(1). Water-impact force signal



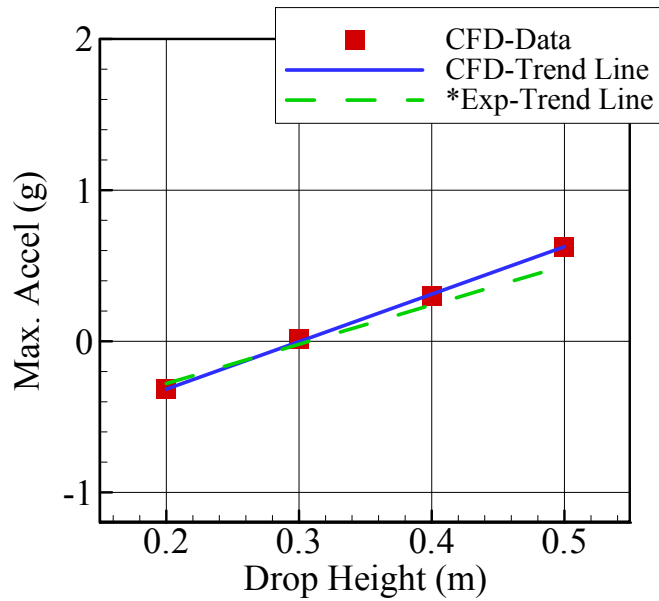
(2). Body acceleration signal



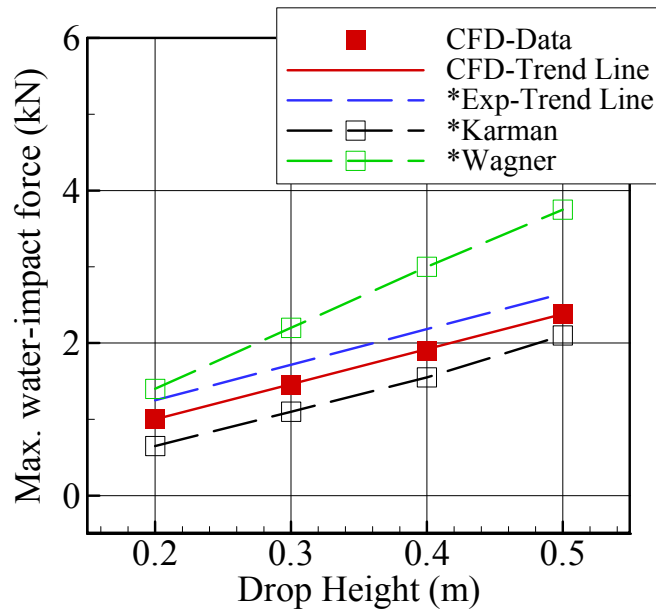
(3). Water-entry depth (z) signal

Fig. 5. 3 Time signals by different drop heights (H)

(For different H , time $t=0$ indicates the instant that hull touches water)



(1). Maximum acceleration value over drop heights



(2). Maximum water-impact force and drop height (*Hong *et al.*, 2012)

Fig. 5. 4 Relationship between maximum value and drop height

Chapter 6 Conclusions

This thesis presents the CFD analysis on two typical phenomena of violent hydrodynamic problems: sloshing and water-entry impact. The work focuses mainly on the observation on hydrodynamic impact characteristics, investigating the parametric sensitivity to computational parameters and the validation of CFD results. Findings and contributions are summarized as follows:

1. The effect of adaptive mesh refinement around impact region is observed in sloshing problem. The appropriate arrangement of refinement zones is proved to reduce computation time significantly and perform good computation.
2. The effect of overset-mesh technique is studied in water-entry problem. It shows that two overlapping meshes communicate the variables at the overset interface by interpolation method, and inappropriate interpolation can introduce variables of extremely oscillating values or even break the computation. The size of overset region and appropriate data mapping are important to apply the overset-mesh technique.
3. The impact pressure is very sensitive to grid size, and a high grid resolution is useful for capturing the exact free-surface profile. For both sloshing and water-entry problems, the impact pressure signals showed a tendency that peak value grows higher and signal becomes smoother as the mesh becomes finer. Moreover, unexpected trapped air and oscillating pressure signals occurred in water-entry problem, but they are considered as numerical error which can be reduced as improvement of grid resolution.
4. Compared with grid size, time step shows relatively much weaker sensitivity

on impact pressure. An appropriate time step should ensure that the maximum CFL value should be less than 1.0 during whole computation. However, oscillatory signal also appears when a too small time-step is used.

5. For the water-entry problem, the present CFD computation shows good performance in high Fn condition. At high Froude number condition, the results showed an excellent correspondence with potential theories. CFD analysis proofed that gravity effect is negligible at high Froude number.
6. An exploration of CFD analysis in 3-D water-entry problem was performed for a modified Wigley model. The linearly proportional relationship was observed between drop height and peak impact force. Moreover, results show that the maximum of impact force occurs at the same water-entry depth, independent of drop height. These impact characteristics correspond well with experiments.
7. This study validated the CFD computations in violent water-impact problems from numerical point of view. Based on this experience, this study can be extent to the analysis of more complicated phenomena, e.g. complicated geometry and water-impact with air pocket.

Bibliography

- [1] Celik, I.B., Ghia, U., Roache, P.J., Freitas, C.J., Coleman, H., and Raad, P.E., 2008, "Procedure for estimation and reporting of uncertainty due to discretization in CFD applications", *Journal of Fluids Engineering*, 130, 078007-078004
- [2] Hong, S.Y., Kim, Y.S., Kyoung, J.H., Hong, S.W., Kim, Y.H., 2012, "Experimental Study on Impact Loads Acting on Free-falling Modified Wigley", *International Journal of Ocean System Engineering*, 2(3), 151-159
- [3] Kim, Y., 2001, "Numerical simulation of sloshing flows with impact load", *Applied Ocean Engineering*, 23(1), 53-62
- [4] Kim, Y., Yang, K.K., Kim, J.H., Zhu, Z., 2016, "Computation of Water-entry Impact of Wedge and Ship-like Section Using Potential Theories and CFD Computations", *Proceedings of the 26th International Ocean and Polar Engineering Conference (ISOPE-2016)*, Rhodes, Greece
- [5] Lee, D.H., Kim, M.H., Kwon, S.H., Kim, J.W., Lee, Y.B., 2007, "A parametric sensitivity study on LNG tank sloshing loads by numerical simulations", *Ocean Engineering*, 34(1), 3-9
- [6] Korea Research Institute of Ships and Ocean Engineering (KRISO), 2014, "Wave Induced Loads on Ships Joint Industry Project-III Report", Report No BSPIS7230-10572-6

- [7] Korobkin, A., 2004, "Analytic models of water impact", *European Journal of Applied Mathematics*, 15, 821-838
- [8] Loysel, T., Gervaise, E., Moreau, S. Brosset, L., 2013, "Results of the 2012-2013 Sloshing Model Test Benchmark", *Proceedings of the Twenty-third (2013) International Offshore and Polar Engineering*, Alaska, USA
- [9] Murthy, J.Y., 2002, "Numerical Methods in Heat, Mass and Momentum Transfer", Springer, Purdue University
- [10] Peric, M., Ferziger, J.H., 2002, "Computational Methods for Fluid Dynamics", Springer, New York
- [11] CD-adapco, 2014, "Star-CCM+ v9.06 User Guide"
- [12] von Karman, T., 1929, "The impact of seaplane floats during landing", NACA TN-321
- [13] Wagner, H., 1932, "Uber Stoss-und Gleitvorgange an der Oberflache von Flussigkeiten", *Z. angew. Math. Mech.*, 12(4), 193-215
- [14] Yang, K.K., Kim, J., Kim, Y., 2015, "Comparison of Sloshing Impact Flows between PIV Measurement and CFD Computation", *Proceedings of the 9th International Workshop on Ship and Marine Hydrodynamics*, Glasgow, UK
- [15] Zhao, R., Faltinsen, O., 1993, "Water entry of two-dimensional bodies", *Journal of Fluid Mechanics*, 246, 593-612

초록

슬로싱 충격과 물체의 입수 충격은 짧은 시간동안 큰 자유수면 변화와 큰 하중을 유발하는 두 가지 대표적인 비선형 문제이다. 전통적으로 동안 실험과 퍼텐셜 이론을 이용하여 많은 연구가 진행되었지만, 본 논문에서는 상용 전산유체역학 (Computational fluid dynamics, CFD) 프로그램, Star-CCM+ 을 슬로싱과 물체의 입수 문제에 적용하였다.

먼저 슬로싱 문제에서 격자 모델의 계산 효율성을 관찰하였다. 충격이 일어나는 영역 주변의 격자를 다르게 구성하였으며 계산 효율성을 높일 수 있는 격자 모델을 설계하였다. 시간 간격과 격자 크기와 같은 계산 인자에 따른 민감도 해석을 통해 수렴된 결과를 얻었으며, 이는 실험과 유사한 압력 신호와 자유수면 형태를 보여주었다.

다음으로 이차원 썰기 및 선박 단면의 입수 문제를 연구하였다. 단면이 계산 영역 내에서 수치학적인 안정성을 잃지 않으며 움직이게 하기 위해서 적절하게 중첩 격자(overlapping mesh)를 배치하였다. 추가로, 높은 프루드수(Froude number, Fn) 조건에서 개발된 해석적인 방법과 비교를 위해서 Fn 의 영향도 관찰하였다. 충격 하중과 자유수면 발달에 있어 CFD 결과가 해석적인 방법과 실험 결과와 비교하였을 때 비슷한 경향성을 보였다.

마지막으로 이차원 입수 문제를 변형된 삼차원 Wigley 선형으로 확장하였다. 최대 선체 가속도와 최대 충격력 모두 낙하 높이에 선형적으로 비례하는 것으로 나타났다. 또한 충격력 최대값이 낙하 높이와 무관하게

같은 입수 깊이에서 관찰되었다. 이런 결과들은 CFD 분석이 공학 분야 적용에 있어 점차 합리적임을 보여준다.

주요어: CFD, 수면충격, 슬로싱, 입수

학번: 2014-25273